



NASA CR -165, 314

NASA-CR-165314  
19810020903

NASA CR-165314  
MTI-81TR8



# DEVELOPMENT OF HIGH-SPEED BALANCING TECHNOLOGY

by

R. DeMuth and Dr. E. Zorzi

**MECHANICAL TECHNOLOGY INCORPORATED**

prepared for

**NATIONAL AERONAUTICS AND SPACE ADMINISTRATION**

NASA Lewis Research Center  
Contract NAS 3-18520  
David P. Fleming, Project Manager

RECEIVED / COPY  
AUG 10 1981

AUG 10 1981

RECEIVED / COPY  
AUG 10 1981  
AUG 10 1981

### **NOTICE**

**This report was prepared as an account of Government-sponsored work. Neither the United States, nor the National Aeronautics and Space Administration (NASA), nor any person acting on behalf of NASA:**

- A. Makes any warranty or representation, expressed or implied with respect to the accuracy, completeness, or usefulness of the information contained in this report, or that the use of any information, apparatus, method, or process disclosed in this report may not infringe privately-owned rights; or**
- B. Assumes any liabilities with respect to the use of, or for damages resulting from the use of, any information, apparatus, method, or process disclosed in this report.**

**As used above, "person acting on behalf of NASA" includes any employee or contractor of NASA, or employee of such contractor, to the extent that such employee or contractor of NASA or employee of such contractor prepares, disseminates, or provides access to any information pursuant to this employment or contract with NASA, or his employment with such contractor.**

**Requests for copies of this report should be referred to  
National Aeronautics and Space Administration  
Scientific and Technical Information Facility  
P.O. Box 33  
College Park, Md. 20740**

NASA CR-165314  
MTI 81TR8

**FINAL REPORT**

**DEVELOPMENT OF  
HIGH-SPEED BALANCING TECHNOLOGY**

by

R. DeMuth and Dr. E. Zorzi

**MECHANICAL TECHNOLOGY INCORPORATED**

968 Albany-Shaker Road  
Latham, New York 12110

prepared for

**NATIONAL AERONAUTICS AND SPACE ADMINISTRATION**

January 1981

Contract NAS 3-18520

**NASA Lewis Research Center  
Cleveland, Ohio**

**David P. Fleming, Project Manager  
Structures and Mechanical Technologies Division**

N81-294411#





1. Report No. NASA CR-165314		2. Government Accession No.		3. Recipient's Catalog No.	
4. Title and Subtitle Development of High-Speed Balancing Technology Part 1 - Effects of Laser Metal Removal on Material Properties Part 2 - Balancing of Supercritical Shaft Under Torque Load				5. Report Date January 1981	
				6. Performing Organization Code	
7. Author(s) R. DeMuth Dr. E. Zorzi				8. Performing Organization Report No. MTI 81TR8	
				10. Work Unit No.	
9. Performing Organization Name and Address Mechanical Technology Incorporated 968 Albany-Shaker Road Latham, New York 12110				11. Contract or Grant No. NAS3-18520	
				13. Type of Report and Period Covered Final	
12. Sponsoring Agency Name and Address National Aeronautics and Space Administration Washington, DC 20546				14. Sponsoring Agency Code	
15. Supplementary Notes Project Manager, David P. Fleming, Structures and Mechanical Technologies Division, NASA-Lewis Research Center, Cleveland, Ohio					
16. Abstract  This report presents the tasks performed in the continuous high-speed balancing technology investigation to (1) determine the effects of laser material removal on material properties and (2) establish a balancing methodology that could control unbalance response with the application of axial torque, evaluate this methodology by experimental testing, and compare predicted and experimental results.  An investigation into laser material removal showed that laser burns act in a manner typical of mechanical stress raisers causing a reduction in fatigue strength; the fatigue strength is lowered relative to the smooth specimen fatigue strength. Laser-burn zones were studied for four materials: Alloy Steel 4340, Stainless Steel 17-4 PH, Inconel 718, and Aluminum Alloy 6061-T6. Calculations were made of stress concentration factors ( $K_t$ ) for laser-burn grooves of each material type. A comparison was then made to experimentally determine the fatigue strength reduction factor ( $K_f$ ). These calculations and comparisons indicated that, except for the 17-4 PH material, good agreement (a ratio of close to 1.0) existed between $K_t$ and $K_f$ . The performance of the 17-4 PH material has been attributed to early crack initiation due to the lower fatigue resistance of the soft, unaged laser-affected zone. This report also contains qualitative discussions of metallography and microhardness profiles of each material's laser-affected zones.  Also covered in this report is the development, implementation, and testing of an influence coefficient approach to balancing a long, slender shaft under applied-torque conditions. This balancing approach takes advantage of the fact that the influence coefficients are not torque dependent; this factor minimizes the number of conditions at which trial weight data must be taken. An evaluation of this method of balancing was performed using a U.S. Army/NASA supercritical power transmission facility. Excellent correlation existed between the analytically predicted results and those data obtained from testing.					
17. Key Words (Suggested by Author(s)) Balancing Flexible Rotor Balancing Laser Metal Removal/Machinery				18. Distribution Statement	
19. Security Classif. (of this report) Unclassified		20. Security Classif. (of this page) Unclassified		21. No. of Pages 93	
				22. Price*	

\* For sale by the National Technical Information Service, Springfield, Virginia 22161



## TABLE OF CONTENTS

<u>SECTION</u>	<u>PAGE</u>
LIST OF FIGURES . . . . .	v
LIST OF TABLES . . . . .	vii
SUMMARY . . . . .	ix
INTRODUCTION . . . . .	xi
ACKNOWLEDGEMENTS . . . . .	xiii

### PART 1

#### EFFECTS OF LASER METAL REMOVAL ON MATERIAL PROPERTIES

1.0	INTRODUCTION TO PART 1. . . . .	1
2.0	DETAILS OF LASER SYSTEM, TEST SPECIMENS, AND LASER MATERIAL REMOVAL . . . . .	3
2.1	Laser System . . . . .	3
2.1.1	Laser Module and Mirrors . . . . .	3
2.1.2	Power Supply . . . . .	3
2.1.3	Test Fixture . . . . .	3
2.2	Procedure for Laser Burns, Cutting Sections and Machining Fatigue Specimens . . . . .	4
2.2.1	Test Specimens - Uniradiated Radius . . . . .	4
2.2.2	Test Specimens - Laser Burn . . . . .	5
3.0	FATIGUE TESTING . . . . .	7
3.1	Objective . . . . .	7
3.2	Experimental Detail . . . . .	7
3.3	Fatigue Test Results . . . . .	8
4.0	METALLOGRAPHY STUDIES . . . . .	9
4.1	Specimen Preparation and Examination Procedures . . . . .	9
4.2	4340, Low-Alloy Steel . . . . .	9
4.3	17-PH, Precipitation-Hardened Stainless Steel . . . . .	10
4.4	Inconel 718, Nickel-Base Superalloy . . . . .	11
4.5	6061-T6 Aluminum Alloy . . . . .	12

TABLE OF CONTENTS (Cont'd)

<u>SECTION</u>		<u>PAGE</u>
5.0	MICROHARDNESS TESTING . . . . .	13
6.0	RESULTS AND DISCUSSION . . . . .	15
7.0	CONCLUSIONS . . . . .	17
8.0	REFERENCES . . . . .	19

PART 2

BALANCING OF SUPERCRITICAL  
SHAFT UNDER TORQUE LOAD

9.0	INTRODUCTION TO PART 2 . . . . .	21
10.0	TEST PROGRAM . . . . .	23
	10.1 Background . . . . .	23
	10.2 Analytic Basis . . . . .	23
	10.3 Program Plan . . . . .	24
11.0	RESULTS AND DISCUSSION . . . . .	27
12.0	RECOMMENDATIONS AND CONCLUSIONS . . . . .	29
13.0	BIBLIOGRAPHY . . . . .	31
	FIGURES . . . . .	33
	TABLES . . . . .	77
	APPENDIX A MATERIAL CERTIFICATIONS . . . . .	87
	APPENDIX B SPECIMEN MACHINING DETAILS . . . . .	91

# LIST OF FIGURES

<u>NUMBER</u>		<u>PAGE</u>
1	Specimen Test Fixture. . . . .	33
2	MTS Fatigue Machine. . . . .	34
3	Inconel 718 Fatigue Data . . . . .	35
4	6061-T6 Fatigue Data . . . . .	36
5	17-4 PH Fatigue Data . . . . .	37
6	4340 Fatigue Data. . . . .	38
7	Laser Burn in 4340 Steel: Surface Profile . . . . .	39
8	Laser Burn in 4340 Steel: Depth Profile . . . . .	40
9	Laser Burn in 4340 Steel: Surface Left in the Trough of the Laser Burn . . . . .	41
10	Microstructure of the Laser Affected Zone in 4340 Steel . . . . .	42
11	Bulk Microstructure of 4340 Steel. . . . .	43
12	Laser Burn in 17-4 PH Stainless Steel: Surface Profile. . . . .	44
13	Laser Burn in 17-4 PH Stainless Steel: Depth Profile. . . . .	13
14	Laser Burn in 17-4 PH Stainless Steel: Surface Left in Trough of the Burn. . . . .	46
15	Bulk Microstructure of 17-4 PH Stainless Steel . . . . .	47
16	Microstructure of the Laser-Affected Zone in 17-4 Stainless Steel Directionally Solidified Martensite. . . . .	48
17	Microstructure of the Laser Affected Zone in 17-4 PH Stainless Steel Martensite-Ferrite Transformation . . . . .	49
18	Laser Burn Inconel 718 . . . . .	50
19	Laser Burn in Inconel 718: Depth Profile. . . . .	51
20	Laser Burn in Inconel 718: Surface Left in the Trough of the Laser Burn . . . . .	52
21	Microstructure of the Laser-Affected Zone in Inconel 718 (Midpoint of Laser Burn) . . . . .	53
22	Microstructure of the Laser-Affected Zone in Inconel 718 (Near End of Laser Burn) . . . . .	54
23	Laser Burn in 6061-T6 Aluminum: Surface Profile . . . . .	55
24	Laser Burn in 6061-T6 Aluminum: Depth Profile . . . . .	56
25	Laser Burn in 6061-T6 Aluminum: Surface Left in the Trough of the Laser Burn . . . . .	57

LIST OF FIGURES (Cont'd)

<u>NUMBER</u>		<u>PAGE</u>
26	Puckering and Microcracking in 6061-T6 Aluminum Laser-Burn Surface . . . . .	58
27	Bulk Microstructure of 6061-T6 Aluminum (From Longitudinal Cross-Section Speciman of Laser Burn. . .	59
28	Microstructure of the Laser-Affected Zone in 6061- T6 Aluminum (At the One-Quarter Distance Point Along Laser Burn). . . . .	60
29	Microstructure of the Laser-Affected Zone in 6061- T6 Aluminum (Near End of Laser Burn) . . . . .	61
30	Sketches of a Laser Cut Sample: Sectioning, Mount- ing and Microhardness Measurements . . . . .	62
31	Microhardness - Depth Profile: 4340 . . . . .	63
32	Microhardness - Depth Profile: 6061-T6. . . . .	64
33	Microhardness - Depth Profile: 17-4 PH. . . . .	65
34	Microhardness - Depth Profile: Inconcel 718 . . . . .	66
35	Drive Train Dynamics Technology Test Rig Configuration for High-Speed Shaft Balancing . . . . .	67
36	View of Completely Assembled Test Rig Showing High- Speed Side from Drive Gearbox End. . . . .	68
37	Elastomer Damper/Squeeze-Film Damper Schematic . . . . .	69
38	First Rotor Critical Speed . . . . .	70
39	Rig Configuration with Instrumentation . . . . .	71
40	Baseline Test Condition - Probe 6. . . . .	72
41	Rotor Response After Balance Correction Applied for Torque Condition - Probe 8 . . . . .	73
42	Rotor Response After Balancing Correction Applied for Torque Condition - Probe 3 . . . . .	74
43	Rotor Response After Balancing Correction Applied for Torque - Probe 5 . . . . .	75
44	Typical Synchronous Response of Power Transmission Shaft as Determined by Torque Loading. . . . .	76

## LIST OF TABLES

<u>NUMBER</u>		<u>PAGE</u>
1	4340 Fatigue Data . . . . .	77
2	17-4 PH Fatigue Data. . . . .	78
3	Inconel 718 Fatigue Data. . . . .	79
4	6061-T6 Fatigue Data. . . . .	80
5	Fatigue Strength Reduction Factors. . . . .	81
6	Comparison of Stress Concentration to Strength Reduction. . . . .	82
7	Baseline Data Figure 40 at 905 rpm. . . . .	83
8	Balanced Rotor Figures 41 and 42 at 905 rpm . . . . .	84
9	Predicted Balancing Data. . . . .	85
10	Influence Coefficient Data Response to Center Plane Trial Weight Location . . . . .	86





## SUMMARY

The purpose of this report is to summarize the results obtained by Mechanical Technology Incorporated (MTI) under Task VII and Task VIII of NASA Contract NAS3-18520.

Under Task VII, four cylindrical test specimens (alloy steel 4130, stainless steel 17-4PH, Inconel 718, and aluminum alloy 6061-T6) were mounted in a test fixture consisting of a 3-jaw lathe chuck, spindle, and variable speed motor. A laser beam was focused on a rotating specimen, and material was removed at a specific angular location. After firing the laser, the test specimens were cut into segments and machined into bars for fatigue testing. Sections were examined to determine the profiles of laser-burn zones, the extent of incipient melting at the laser zone, and the degree and extent of microstructural alterations in the heat-affected zones. Microhardness profiles were made of the heat-affected zones.

A series of high-cycle fatigue tests were conducted to determine what effect the laser burn would have on the fatigue strength of the specimens. Baseline fatigue tests were made on each material using smooth, polished specimens. By comparing the fatigue strength of the laser-burned specimens to the smooth specimen fatigue strength, the effect of the laser burn was established. In all cases, the laser burn reduced the fatigue strength by a factor ranging from 3 (for Inconel 718) to a reduction of over 7 (for the stainless steel 17-4PH). A reduction in fatigue strength caused by the laser burn is not unexpected, as any mechanical stress raiser, such as a keyway or fillet, will lower the fatigue strength relative to the smooth specimen fatigue strength.

The calculated stress concentration values ( $K_t$ ) were estimated for each material laser-burn groove so that a comparison could be made with the experimentally determined fatigue strength reduction factors ( $K_f$ ). Except for 17-4PH material, this comparison showed good agreement between  $K_t$  and  $K_f$ , considering the assumption of the idealized shape of the laser burn groove. The variation of the 17-4PH material is explained by variation in hardness change and microstructure of the laser zone.

Under Task VIII of this contract, a method for balancing of a long, slender, supercritical shaft was developed and implemented. The 3.66 m (12 ft) long aluminum shaft, with a 7.61 cm (3 in.) diameter and a wall thickness of 3.2 mm (0.125 in.), was operated on an ARMDL/NASA test facility located at Mechanical Technology Incorporated (MTI) in Latham, N.Y. Previous testing of the shaft had demonstrated that the synchronous vibration always increased when the torque level was altered from that value of torque applied during balancing. Prior testing also indicated that the influence coefficients were not torque dependent.

The approach used in this contract was to develop a weighted least-squares solution to the influence coefficient balancing problem. This required a modification of the general balancing equation, by including a superposition of the response at both torque conditions. By taking advantage of the fact

that the influence coefficients are not torque dependent, the solution form minimizes the number of conditions at which trial weight data must be taken.

Operating the shaft through the first bending critical speed at 110 N/m (1,000 in.-lb) increment of torque to a maximum of 900 N/m (8,000 in.-lb) demonstrated excellent correlation between predicted analytic results and test data.

## INTRODUCTION

The results presented in this report are a continuation of flexible rotor balancing technology at Mechanical Technology Incorporated (MTI), presented in "Balancing Techniques for High-Speed Flexible Rotors" (NASA CR-2975) and "Experiments on Multiplane Balancing Using a Laser for Material Removal" (NASA CR-3105). These previous tasks demonstrated and proved the multi-plane-multispeed method for flexible rotor balancing. Also demonstrated was the ability to add a laser for material removal and to automate removal process, such that the rotor could remain at speed.

This report presents the tasks performed in the continuing high-speed balancing technology investigation to:

- Determine the effects of laser material removal on material properties by performing metallographic and mechanical property testing
- Establish a balancing methodology which could control unbalance response with the applications of axial torque; evaluate this methodology by experimental testing; compare predicted and experimental results.

The test procedures, results, recommendations and conclusions are presented herein.



### ACKNOWLEDGEMENTS

The authors would like to acknowledge the work of Mr. Leonard Kaisand, Senior Mechanical Metallurgist, for the fatigue testing and Dr. Gerald Stelma, Materials Scientist, for metallography and microhardness testing.



Part 1

Effects of Laser Metal Removal  
on Material Properties

**This Page Intentionally Left Blank**



## 1.0 INTRODUCTION TO PART 1

The ability to use laser material removal for rotor balancing [ref. 1] demonstrated that:

- The procedure can successfully balance rotating shaft-systems by use of a computer control system
- The accurate control of the angular and axial position of the material removal zone can be demonstrated
- Increased removal rates can be anticipated with continuing laser development
- The removal rate has a limiting maximum surface speed related to the laser energy and pulse duration.

The principal area not evaluated in previous contracts was that of the metallurgical effects on the material removal zone. These effects would be important in the use of laser removal techniques in production balancing to assure that no harm would occur to the material in the balancing removal zone.

Part 1 of this report summarizes the metallurgical results of four materials examined to determine the laser burn profiles, extent of incipient melting at cut surfaces, degree and extent of microstructural alterations, micro-hardness profiles. Fatigue tests were performed to determine the mechanical properties of each specimen.

**This Page Intentionally Left Blank**

## 2.0 DETAILS OF LASER SYSTEM, TEST SPECIMENS, AND LASER MATERIAL REMOVAL

### 2.1 Laser System

The laser system used for the material removal was a specially modified Model 11C from Laser Incorporated Division of Coherent Radiation, Sturbridge, Massachusetts. The unit is a reliable system, capable of 40 joules of output at a rate of 30 pulses per minute. The 11C System consists of two major subassemblies:

- Laser Module and Mirrors
- Power Supply.

#### 2.1.1 Laser Module and Mirrors

The laser module consists of a water-cooled dielectric tube which contains two high-pressure xenon-filled flashlamps, a phosphate-base neodymium glass laser rod, a silver reflector, and a filter tube. The filter tube protects the laser rod from ultraviolet light produced by the lamps. In operation, both flashlamps and laser rods are cooled with deionized water which flows through the cavity via water connections contained in the outer dielectric housing. The laser mirror assemblies are constructed from aluminum and feature a three-point, spring-loaded suspension system. Nylon dust covers are mounted on both assemblies and extend to the laser rod for dust protection.

Laser Specifications- Laser specifications are as follows:

Lasing Wavelength: 1.06 micrometers  
Energy Output: 40 joules at 30 pulses per minute,  
.9 millisecond duration

#### 2.1.2 Power Supply

The power supply serves the functions of:

- Including operation controls for firing the flashlamps and safety interlocks
- Providing energy storage, necessary for excitation of the laser rod, by a transformer, capacitors and inductor network
- Providing the laser cooling system consisting of pump, heat exchanger, filters and deionizer.

The power supply is completely solid state with maximum charging voltage of 4 kilovolts.

#### 2.1.3 Test Fixture

The laser module assembly was mounted on an optical table driven by a stepping motor. Details of the fixture is shown in figure 1.\* Also shown is a spindle and 3-jaw lathe chuck where the specimens were installed. A variable-speed motor provided a means of gradually increasing the rotational speed. The stepping motor on the optical table allowed the laser beam to be centered on the specimen. Focussing of the beam was accomplished by a movable lens.

---

\*Figures are presented in chronological order beginning on page 33.

A 1-milliwatt helium neon laser provided the focussing beam. The helium neon laser was aligned such that the beam was coaxial with the neodymium glass rod.

The computer control system used to control the laser is described in detail in reference 1 of the bibliography, Section 13.0. A PDP 11/34 computer and associated laser control electronics allow for firing the laser at a specified angular location on the specimen. A computer program allowed the operator to take repeated shots at a specified location.

## 2.2 Procedure for Laser Burns, Cutting Sections and Machining Fatigue Specimens

The following procedures outline the method used to produce specimens for the fatigue testing machine. The sketches appear in appendix B.

### Radius Specimen

- Receive rough machine forgings
- Rough machine (diameters) all material to sketch SK-7036
- Saw into 10 pieces on radial line through center of cylinder
- Follow grinding procedure - Final machine to sketch SK-7037
- Perform fatigue testing.

### Laser-Burn Specimen

- Receive rough machine forging
- Rough machine (diameters) all material to sketch SK-7036
- Install in laser firing fixture, rotate and fire at 10 angular locations or burn zones. Fire 5 shots at each angle for aluminum and fire 10 shots at each angle for remaining materials
- Saw into 10 pieces on radial line through center of cylinder
- Final machine to sketch SK-7038
- Perform fatigue testing.

#### 2.2.1 Test Specimens - Unirradiated Radius

To provide baseline data, test specimens were fatigue tested without being laser-irradiated. The specimens were prepared from forgings of the following materials:

- Alloy Steel, AISI 4340
- Stainless Steel, Type 17-4PH
- Inconel 718
- Aluminum Alloy 6061-T6

Metallurgical reports for these materials are in appendix A.

The materials were purchased as rough machined forgings of 15.88 cm (6.25 in.) outside diameter (O.D.) and 10.16 cm (4.00 in.) inside diameter (I.D.). The cylinder specimens were finish machined to the dimensions shown in appendix B.

From the finish machined cylinders, the radius specimens for fatigue testing were cut by segmenting the cylinders into 10 pieces. In order to provide a high stress area for fatigue testing, the segments were machined into bars 2.86 cm x 2.22 cm (1.125 x .875 in.) by approximately 15.24 cm (6 in.), and a large radius (7.61 cm (3 in.)) ground in the center of each specimen. Details of the machining dimensions are shown in appendix B.

#### 2.2.2 Test Specimens - Laser Burn

Finish machined cylinders were placed in a fixture consisting of a 3-jaw lathe chuck, supported by a Whitton spindle and driven by a variable-speed motor. The spindle was mounted to a table which also supported the laser module.

The laser focussing lens was 76 cm (30 in.) from laser rod, and a 10 diopter focal point lens was used. The specimens were rotated at 1000 rpm; 5 laser shots were made for the aluminum specimens; and 10 shots for the remaining materials. The power supply voltage setting was 3.00 kilovolts and .9 milli-second pulse duration. From each cylinder, 10 specimens were made by controlling the burn zones at 36-degree increments.

**This Page Intentionally Left Blank**

### 3.0 FATIGUE TESTING

#### 3.1 Objective

A series of high cycle fatigue (HCF) tests were conducted to determine what effect the laser burn would have on the HCF strength of four typical structural materials (Alloy Steel 4340, Stainless Steel 17-4 PH, Inconel 718, Aluminum Alloy 6061-T6).

This effect was established by first conducting baseline fatigue tests on each material using smooth, polished specimens. Fatigue tests were then conducted on test specimens containing the groove left after the material was removed by the laser burn. By comparing the HCF strength of the laser-burned specimens to the smooth specimen fatigue strength, the effect of the laser burn was established for each investigated material.

#### 3.2 Experimental Detail

All fatigue tests were conducted in direct four-point bending using a 20-Kip MTS fatigue machine. Figure 2 shows the four-point bending fixture and a smooth test specimen in the MTS fatigue machine. Load was the controlled parameter; the magnitude of the load was determined by the desired value of bending stress to be applied to each specimen. The load required for a given bending stress was calculated using the following equation.

$$P = \frac{2 I S_{\max}}{l_c}$$

where

P = Applied load

$S_{\max}$  = Maximum outer fiber bending stress

c = Distance from neutral axis to outer fiber

l = Moment arm (2" for this setup)

I = Moment of inertia for test region cross section.

This equation is the flexure formula solved for applied load. Each test was conducted at an R ratio (ratio of minimum stress to maximum stress) of 0.05; therefore, the controlled stress range,  $\Delta S$ , was 0.95 times  $S_{\max}$ . The waveform was sinusoidal. Each individual test was conducted at a constant frequency of cycling. However, the frequency varied from 10 Hz to 28 Hz depending on the magnitude of the applied load and the resulting specimen deflection. At high loads and large deflections, the lower test frequencies were used to stay within the performance capabilities of the test machine. Since all tests were conducted in air at room temperature, no frequency effect would be expected. For these materials and test conditions, a frequency greater than about 170 Hz would have to be exceeded before a frequency effect would be expected. (See ASTM standard E466, Section 7.4.)

### 3.3 Fatigue Test Results

The fatigue data from both the baseline smooth specimens and the laser-burned specimens are presented in tables 1\* to 4 for each of the four materials investigated. These data are plotted as  $S_{\max}$  versus cycles to failure,  $N$ , in figures 3 through 6. Each figure contains all fatigue data for a particular material. The upper S-N curve (circular symbols) is the smooth radius specimen baseline data, and the lower S-N curve (triangular points) is the laser-burned specimen data.

The S-N curves in these figures were obtained by least squares fitting the data to the linear relationship,

$$\text{LOG}(N) = A + B \text{ LOG}(S_{\max})$$

where  $A$  and  $B$  are the intercept and slope, respectively. This expression, containing the particular values of  $A$  and  $B$  obtained by the linear regression, is presented for each set of data along with the correlation coefficient as a measure of dispersion. These S-N curves are for a 50% survival if the logarithms of the lives are described by a log normal distribution. No run-out data were included during the linear regression analysis. However, the data were taken into account when it was obvious that the complete S-N curve was more appropriately described by two straight lines where one line is horizontal at the fatigue limit.

For the purpose of comparing data, the fatigue strength was taken as the stress required to cause failure in  $10^7$  cycles, as determined by the fitted S-N curves. Table 5 contains the fatigue strengths at  $10^7$  cycles for each material. The last column in this table lists the fatigue strength reduction factors,  $K_f$ , defined as the ratio of smooth specimen fatigue strength to the laser-burned fatigue strength for a given material. In all cases, the effect of the laser burn was to reduce the fatigue strength by a factor ranging from 3 for Inconel 718 to a reduction of over 7 for the stainless steel 17-4 PH.

---

\*Tables begin on page 77.



## 4.0 METALLOGRAPHY STUDIES

### 4.1 Specimen Preparation and Examination Procedures

Two laser-burn specimens from each test material were taken for metallographic examination. One specimen was examined "as is" to document

- by macrophotography, the burn profile produced in the surface of the test material
- by scanning electron microscopy, the morphology of the surface left in the trough of the burn.

The laser cut specimens, which were sectioned to show the profile of the laser cut and the microstructure, were prepared by first applying a layer of electroless nickel to preserve the fine features of the laser-affected surfaces. The specimens were then cut to expose the desired profile through the laser cut and mounted in a standard epoxy mounting material. Particular attention was paid to maintaining a flat surface for microscopic examination during the subsequent grinding and polishing. The profile surface prepared in this manner was etched with a 2 percent nitric acid in ethanol solution (Nital-2%).

A metallographically prepared longitudinal cross section of the burn was made from the other specimen and was used to document, by light microscopy

- the depth profile of the burn
- the extent of the laser-affected zone (LAZ)
- the condition of the metallurgical microstructure in the LAZ.

The laser-burned test materials were

- (1) 4340, low alloy steel
- (2) 17-4 PH, precipitation-hardened stainless steel
- (3) Inconel 718, nickel-base superalloy
- (4) 6061-T6 aluminum alloy.

### 4.2 4340, Low-Alloy Steel

Figures 7A and B are the macrographs taken of a 4340, low alloy steel laser-burn specimen. The burn proceeds from left to right and is in the shape of a teardrop. The dimensions of this burn are

- Width: 0.055 in. (at widest point)
- Length: 0.401 in.

Figures 8A and B are the macrographs taken of the longitudinally sectioned laser-burn specimen. Figure 8A shows the cross section before mounting and metallographic preparation; figure 8B shows the cross section after mounting and metallographic preparation. The burn goes from left to right and the depth profile is approximately elliptical in cross section. The dimensions of this burn are

- Length: 0.329 in.
- Depth: 0.047 in. (at deepest point)

Figure 8A also shows that drops of molten metal have splashed back and frozen onto the wall of the burn trough. These drops are more apparent in the

scanning electron microscope view in figure 9, which is a view looking down into the trough of the laser burn shown in figure 7. The laser burn goes from bottom to top in the photographs. The widest part of the laser burn is approximately at the center of figure 9. The solidified surface of the trough appears smooth and has no microcracks.

Figures 10A and B are micrographs of the microstructure of the laser-affected zone (LAZ). The area shown is at the midpoint (beginning to end) of the laser burn in the longitudinal specimen shown in figure 8B. The white layer is the protective nickel plate put on as part of the metallographic preparation. The average depth of the LAZ is approximately 0.00126 in.

The structure of the LAZ is "as quenched" martensite with some directional solidification of the martensite laths. Evidence of this is shown by the parallel diagonal laths in the LAZ in figure 10B.

The structure of the bulk metal below the LAZ is oil-quenched martensite which has a significant amount of nonmetallic inclusions. Figure 11A shows an etched area of the bulk showing the martensitic structure, and figure 10B is an "as polished" area which was water-rinsed (produces halo artifact) to accentuate the presence of the numerous nonmetallic inclusions.

#### 4.3 17-PH, Precipitation-Hardened Stainless Steel

Figures 12A and B are the macrographs taken of a 17-4 PH stainless steel laser-burn specimen. The burn goes from right to left and is elliptical. The dimensions of this burn are

- Width: 0.054 in. (at widest point)
- Length: 0.402 in.

Figure 13 is the macrograph taken of the metallographically mounted and prepared longitudinal cross section. The burn also goes from right to left, and the depth profile is approximately elliptical in cross section. The dimensions of the burn are

- Length: 0.329 in.
- Depth: 0.052 in. (at deepest point).

Figure 14 is the scanning electron microscope (SEM) view looking down into the trough of the laser burn shown in figure 12. The laser burn goes from bottom to top in the photos, and the widest part (approximately 1/4 the distance from beginning to end of the burn) is approximately at the center of the figure. Drops of molten metal that have splashed back and frozen onto the walls of the trough are again evident. This solidified surface appears smooth and has no microcracks.

Figure 15 is a micrograph of the bulk microstructure of the 17-4 PH stainless steel in the longitudinal cross-section specimen shown in figure 13. The structure is low-carbon martensite (with some delta-ferite), which contains the complex strengthening precipitate resulting from the aging treatment.

Figures 16A and B are micrographs of the microstructure in the LAZ, approximately at the midpoint (beginning to end) of the laser burn. The average thickness of the LAZ is 0.00071 in. The structure is directionally solidified martensite. The martensite grains have grown epitaxially from the bulk grains,

as shown more clearly in figure 16B. The structure is also unaged and untempered and "as quenched."

Cross sections of some drops, such as those evident in the SEM view in figure 14, are seen at the middle left of figure 16A and middle right of 16B. At the very end of the trough and laser burn, there was insufficient heat to melt the metal but enough to transform the preexisting martensite to ferrite (larger, rounder grains). Figures 17A and B show the extent of the ferrite transformation.

#### 4.4 Inconel 718, Nickel-Base Superalloy

Figures 18A and B are the macrographs taken of an Inconel 718 laser-burn specimen. The burn goes from right to left and has an elliptical outline. The dimensions of this burn are:

- Width: 0.055 in. (at widest point)
- Length: 0.473 in.

Figure 19 is the macrograph taken of the metallographically mounted and prepared longitudinal cross section. The burn also goes from right to left. The depth profile is asymmetrical, being deeper at the beginning and gradually becoming more shallow toward the end. The dimensions of this burn are

- Length: 0.329 in.
- Depth: 0.049 in. (at deepest point)

Figure 20 is the scanning electron microscope view looking down into the trough of the laser burn shown in figure 18. The laser burn goes from bottom to top in the photographs, and the point approximately 1/4 of the distance from the beginning to the end of the burn is approximately at the center of the figure. Again, drops of molten metal that have splashed back and frozen onto the walls of the trough are evident. However, the solidified surface appears pimpled and puckered in some areas and some microcracks are present; see photograph #E2610, center. This puckering and cracking may be due to the TiAl brittle oxide film forming on the molten metal before resolidification. This condition might be avoided if the burn were conducted in a vacuum or an inert gas atmosphere, such as helium or argon.

Figures 21A and B are micrographs of the microstructure in the LAZ, approximately at the midpoint (beginning to end) of the laser burn. The average depth of the LAZ is approximately 0.00071 in. The structure of the bulk Inconel 718 beneath the LAZ is a wrought gamma matrix with gamma prime precipitates. The structure of the LAZ is "as cast" gamma solid solution with no gamma prime. Cross sections of some drops, as evident in the SEM view in figure 20, are seen in the middle of Figure 21A.

Figures 22A and B show the LAZ from near the end of the burn. In this region, columnar growth in the solidified LAZ is more evident. This is especially evident in figure 22A. Furthermore, insufficient heat was developed to completely dissolve the titanium carbonitride particle evident in the center of figure 22A and other smaller ones evident in the LAZ of figures 22B and 21B. However, all gamma prime appears to have dissolved (indicated by white color instead of darkening gray as in the bulk).

#### 4.5 6061-T6 Aluminum Alloy

Figures 23A and B are the macrographs taken of one of the 6061-T6, aluminum alloy, laser burn specimens. The burn proceeds from left to right and is in the shape of a teardrop. The dimensions of this burn are

- Width: 0.064 in. (at widest point)
- Length: 0.470 in.

Figures 24A and B are the macrographs taken of the longitudinally sectioned laser-burn specimen. Figure 24A shows the cross section before mounting and metallographic preparation; figure 24B shows the cross section after mounting and metallographic preparation. The burn goes from left to right and the depth profile is approximately semicircular in cross section. The dimensions of the burn are

- Length: 0.329 in.
- Depth: 0.094 in. (at deepest point).

Figure 24A also shows the drops of molten metal that have splashed back and frozen onto the wall of the burn trough. These drops are more apparent in the scanning electron microscope view in figure 25, looking down into the trough of the laser burn shown in figure 23. The laser burn goes from bottom to top in the photographs. The widest part of the laser burn (approximately 1/4 the distance from the beginning to the end of the burn) is approximately at the center of the figure. The solidified surface of the trough appears pimpled and puckered and has microcracks. The puckering and microcracking is shown more clearly in the SEM micrographs of figures 26A, B and C. The puckering and cracking may be due to the brittle oxide film forming on the molten metal before resolidification. This condition might be avoided if the burn were conducted in a vacuum or in an inert gas atmosphere such as helium or argon.

Figure 27 is a micrograph of the bulk microstructure of the 6061-T6 aluminum in the longitudinal cross-section specimen shown in figure 24B. The structure consists of  $Mg_2Si$  (black particles) and  $Fe_3SiAl_{12}$  precipitates (grey dots) in a matrix of aluminum solid solution.

Figures 28A and B are micrographs of the microstructure in the LAZ, approximately at 1/4 the distance from beginning to end of the laser burn. The average depth of the LAZ is approximately 0.00157 in.

The microstructure of the LAZ in this region consists of  $Fe_3SiAl_{12}$  particles directionally segregated in parallel strings in a matrix of cast-aluminum solid solution. No  $Mg_2Si$  particles are evident. Apparently, the  $Fe_3SiAl_{12}$  precipitates did not dissolve in the molten metal, and the  $Mg_2Si$  particles did dissolve.

Near the end of the trough and end of the laser burn, this radical segregation did not occur, as shown in figures 29A and B. Only a little clumping together of the  $Fe_3SiAl_{12}$  is evident in figure 29A.

A cross section of one of the drop blobs, as evident in the SEM view in figure 25, is seen in the middle of figure 29B.

## 5.0 MICROHARDNESS TESTING

The hardness of the LAZ produced in four test materials, which had been subjected to a typical laser balancing burn, has been determined. Microhardness measurements were taken as a function of depth into the test materials. The measurements were performed on metallographically mounted, polished, and etched longitudinal cross sections of each laser cut. Figure 30 shows sketches of the laser-burn sample, how it was sectioned and mounted, and from where the microhardness measurements were taken. The test materials were

- 4340 low-alloy steel
- 17-4 PH precipitation-hardened stainless steel
- Inconel 718 nickel-base superalloy
- 6061-T6 aluminum alloy.

Figures 31, 32, 33 and 34 are the respective hardness-depth profiles obtained for these samples. A Knoop hardness indenter was used and, therefore, the hardness values are reported in KHN (Knoop Hardness Number).

The 4340 steel was the only material to have the laser-affected zone harder than the bulk. The laser-affected zone in all three other materials was found to be softer than the bulk material. In all cases, the laser affected the hardness of the materials only as deep as the heat-affected zones, which in all cases, were readily identified by microscopic examination of the etched cross sections. The depth of the LAZ in each material, determined by microscopic examination, was

- 4340: 1.26 mil
- 17-4PH: 0.71 mil
- Inconel 718: 0.71 mil
- 6061-T6: 1.57 mil.

The 4340-steel laser-affected zone is harder than the bulk because of the extremely rapid quench from the liquid to the solid state, producing "as quenched" martensite. A tempering heat treatment would be required to bring the laser-affected zone back to a metallurgical state similar to that of the bulk.

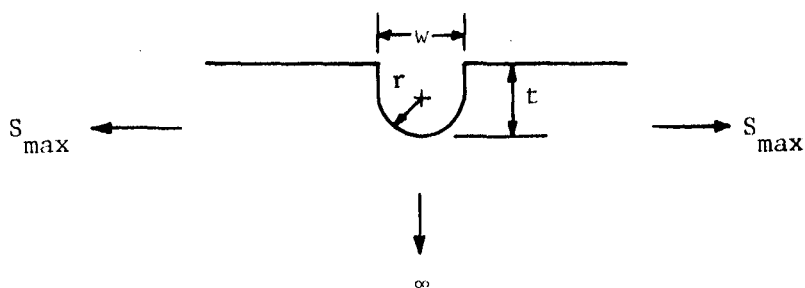
All three other materials rely on the aging (growth) of precipitates in the solid phase to increase their strength and hardness. These precipitates were believed to have dissolved in the molten liquid metal, and the rapid quench was believed to have frozen them into a state of solid solution. Therefore, an aging heat treatment would be required to bring the laser-affected zone back to a state similar to that of the bulk.

**This Page Intentionally Left Blank**

## 6.0 RESULTS AND DISCUSSIONS

A reduction in fatigue strength caused by the laser burn is not unexpected, as any mechanical stress raiser, such as a keyway or fillet, will lower the fatigue strength relative to the smooth specimen fatigue strength. The amount of the reduction would depend on the elastic stress concentration,  $K_t$ , for the groove left by the laser burn. For the high strength materials investigated, it is reasonable to expect the fatigue strength reduction factor,  $K_f$ , to be nearly equal to  $K_t$ .

Estimates were made of the stress concentration,  $K_t$ , for each material's laser-burn groove so that a comparison could be made to the experimentally determined fatigue strength reduction,  $K_f$ , listed in table 5. These estimates were made assuming the laser burn to be a shallow elliptical notch in an infinitely wide body as shown below.



The expression [2] for calculating the stress concentration factor in bending for this configuration is

$$K_t = 1 + 2 \sqrt{t/r}$$

This expression was used to calculate the stress concentration,  $K_t$ , for each material's laser groove using the appropriate dimensions presented in section 4.0. The radius,  $r$ , was assumed to be one-half the width,  $w$ , of groove at the surface of the specimen.

A comparison of the calculated values of  $K_t$  and  $K_f$  obtained experimentally is made in table 6. Except for the 17-4 PH material, this comparison shows good agreement between  $K_t$  and  $K_f$ , considering the assumption of the idealized shape of the laser-burn groove.

The comparison made in the previous paragraph is based purely on the geometry of the laser burn and does not consider the microstructure and hardness change in the LAZ. A qualitative discussion follows that shows how taking the LAZ into consideration might effect the comparisons of  $K_t$  and  $K_f$  for 17-4 PH.

The fatigue strength reduction factor,  $K_f$ , was almost 2 times the calculated stress concentration factor,  $K_t$ , for 17-4 PH. This difference is too great to be attributed solely to the lack of exactness in the  $K_t$  calculation. The difference probably can be attributed to early crack initiation because of the lower fatigue resistance of the soft, unaged LAZ. Thus, the measured "fatigue strength" represents the threshold for propagating a crack into the nonlaser-affected material, which is hard, aged 17-4 PH. If this is indeed the case, the laser burn and cracked LAZ should be analyzed using fracture mechanics. The appropriate parameter to be considered is the threshold range of stress intensity factor,  $\Delta K_{th}$ , rather than the stress concentration factor. The stress intensity factor,  $K$ , is the magnitude of the ideal crack-tip stress field in a linear-elastic body. In fatigue-type loading, the stress-intensity factor range,  $\Delta K$ , is the variation in the stress-intensity factor during the fatigue cycle; that is,  $K_{max} - K_{min}$ . The threshold range of the stress intensity factor,  $\Delta K_{th}$ , is a minimum value of  $\Delta K$  below which a fatigue crack will not propagate and is a material property.

Assuming the laser burn to be a semi-elliptical surface flaw, a  $\Delta K_{th}$  of 6.8 Ksi $\sqrt{\text{in.}}$  was calculated. This value is consistent with what would be expected for a high-strength steel although no threshold data was found in the literature specifically for 17-4 PH. However, considerable threshold data exists for 4340, with reported  $\Delta K_{th}$  values ranging from 4 to 6 Ksi $\sqrt{\text{in.}}$ , depending on the strength level of the 4340 tested. The calculated  $\Delta K_{th}$  of 6.8 Ksi $\sqrt{\text{in.}}$  compares well with this range of values for 4340. This is a valid comparison, as  $\Delta K_{th}$  is fairly constant within a given class of material, such as high-strength steels, aluminum alloys, etc.



## 7.0 CONCLUSIONS

The goal of the physical appearance of the laser-burn zone is to duplicate the appearance of the machine or hand grinding technique done by the operator. Typical removal zones specified by hand grinding have a zone specified by a not-to-exceed depth and a shape shown on a drawing. By experience, the operator of the balancing equipment has a feel or instinct for the amount of correction and the size or depth of removal. The technique of the operator has been developed by the quantity of units that are in production.

The results of the metallurgical investigation have been based on a single burn zone or notch. In high-speed applications, the removal zone is a blended area, where particular attention is applied to the shape, smoothness, and appearance. Balancing of electric motor armatures (low speed) typically uses a notch on a single pole or pair of poles between the windings. This notch results from using a thin grinding wheel as a removal tool. For the initial metallurgical studies, a single groove or notch for burn profile was used.

The method for producing a wide or blended laser removal zone has not been developed to a point of satisfaction because of the many parameters which interact in the removal process and because of the lack of experimental investigation of these parameters. Several of these parameters are:

- Lens Diopter/Focal Length
- Beam Diameter
- Energy Level
- Pulse Duration
- Surface Speed
- Material Properties
- Laser Type
- Repetition Rate.

The future experimental investigations that show promise are: to integrate computer control of the laser energy level and to position the lens by use of a device to adjust the lens-to-target distance.

After experimental methods can be developed to produce a wide and smooth burn zone, future metallurgical investigations can be conducted. An important area would be to compare a wide hand-ground zone to a duplicated zone shape produced by the laser. The laser zone would be tailored to duplicate a smooth surface removal zone.

The neodymium glass laser has a low repetition rate; studies have not been made using another laser type (YAG, Ruby) where the repetition rate is higher. Generally, the laser would produce more pulses at lower energy levels. Removal rates have not been investigated for higher repetition rates.

From the results of table 6, a comparison of the experimental elastic stress concentration factors  $K_t$ , with the calculated fatigue strength reduction factors  $K_f$ , indicates close agreement, with the exception of the 17-4PH material, as explained in the discussion.

## 8.0 REFERENCES

1. DeMuth, R.S., "Experiments on Multiplane Balancing Using a Laser Material Removal," NASA Contractor Report 3105.
2. Peterson, R.E., "Stress Concentration Design Factors," John Wiley & Sons, Inc., New York, 1953, p. 136.

**This Page Intentionally Left Blank**

Part 2

Balancing of Supercritical  
Shaft Under Torque Load

**This Page Intentionally Left Blank**

## 9.0 INTRODUCTION TO PART 2

The concept of operating power transmission shafts at speeds above the lateral flexural critical speed (supercritical operation) is not new. Industry has long recognized the trade-off that designers have been compelled to make in performance, payload, life, reliability, and cost because of the limitations of rotor-dynamic supercritical shafting technology. The defense industry, in particular, would derive clear advantages in developing supercritical shafting technology. STOL Aircraft, helicopters, turbo-fan engines, and marine power trains, along with numerous other products, would be significantly and directly impacted by supercritical shafting technology.

The advantages of a long, slender shaft over the assembly of short, heavy shaft segments are significant in reducing the number of bearings, reducing the number of couplers, reducing envelope requirements, and reducing cost and maintenance. But, also significant are the past and present technology barriers which have prevented full utilization of the supercritical power concept.

Under a joint Army/NASA- and MTI-funded program, a supercritical power transmission test facility was designed, installed, and operated at MTI. The program goals were to develop the necessary technology for reliable supercritical shafting by providing verification of existing rotor-dynamic capabilities and by assessing the limitations of current technology. The overall objective was to simulate realistic helicopter drive train configurations. This required that the rig be designed and properly instrumented for evaluation of practical geometries (shaft, length, diameter, bearing span, etc.) and run at realistic speeds with applied torque. The purpose of this program has been to generate technology and reduce it to practical terms to permit user-oriented assimilation for product improvement.

Evaluation of power transmission shafting for high-speed balancing has shown that, when axial torque is applied, the imbalance response is altered. An increase in synchronous excitation always occurs if the axial torque level is altered from that value used during balancing. This was the case even if the shaft was balanced with torque applied. The twisting of the long slender shaft produces a change in the imbalance distribution sufficient to disrupt the balanced state.

To deal with this problem, this program was designed to have the following objectives:

- Establish a balancing methodology which could control unbalance response with the application of axial torque
- Evaluate this methodology by balancing the supercritical shaft under axial torque levels
- Compare predicted and experimental results.

This report presents a review of the analytic development of a weighted least-squares approach to influence coefficient balancing and a review of experimental results. The analytic approach takes advantage of the fact that past

testing has shown that influence coefficients are not significantly affected by the application of axial torque. The 3.60-m (12 ft) long aluminum shaft, 7.62 cm (3 in.) in diameter was run through the first flexural critical speed at torque levels ranging from zero torque to 900 N·m (8000 lb-in.) in 110 N·m (1000 lb-in.) increments. The program was successful in meeting all program objectives and in clearly demonstrating excellent correlation between predicted and measured responses.



## 10.0 TEST PROGRAM

### 10.1 Background

To perform this work, the supercritical shaft test facility was used [1].\* A sketch of the test rig is presented in figure 35. A 224-kW (300 horsepower) electric motor is the prime mover for this test rig. The motor drives a variable-speed magnetic coupling with an output speed continuously variable from 50 to 3600 rpm. A gearbox with a ratio of approximately 5.7 to 1 is used to produce a drive shaft speed of up to 20,000 rpm. The drive shaft is formed from a section of aluminum tube 7.6 cm (3 in.) in diameter and 3.66 m (12 ft) long with a 3.2 mm (0.125 in.) wall thickness. Seven balance rings are mounted on the tube at equally spaced intervals to provide for the addition of balance weights to the shaft. Adapters are mounted on the ends of the tube for coupling-to-bearing supports. The coupling adapters are connected to ball-bearing-supported stub shafts by means of disk-type, high-speed flexible couplings. Eddy-current-type displacement probes were used to measure the synchronous and nonsynchronous vibration of the test (drive) shaft. The gearbox is capable of exerting torque to 900 N m (8,000 in.-lb) on the shaft.

The test rig was initially run in this configuration with no external damping other than that provided by the damping in the ball bearings and the air drag on the test shaft. At a later time, an oil squeeze-film damper was added to the test rig to provide significant external damping [2]. The damper was installed at the far end of the test shaft (away from the driving gearbox). A photograph of the test rig with the damper installed is presented in figure 36. Subsequent modification to the rig included an elastomer damper (NASA contract NAS3-18546) in place of the squeeze film. The elastomer damper consisting of six Viton-70 "buttons" was the subject of another study but was operational throughout all phases of this testing. All oil was drained from the squeeze film (and it was flushed with toluene and acetone) when the elastomer damper was used. Figure 37 illustrates the squeeze film damper and elastomer replacement used during this testing. The Viton-70 buttons were 0.64 cm (0.25 in.) in diameter and 0.64 cm (0.25 in.) high. Six buttons, three equally spaced on each end, provided a stiffness of approximately  $8.7 \times 10^5$  N/m (5,000 lb/in.) with a loss factor of 0.75 used for design purposes.

### 10.2 Analytic Basis

One fact surfaces during early testing of the supercritical power transmission shaft, i.e., the influence coefficients did not change when torque up to 900 N m (8,000 in.-lb) was applied. Obviously, this is a significant result in a number of ways. If a point speed approach [3] was to be used, then the effect of torque, if assessed similar to the method of balancing at multiple speeds, would produce a singular influence coefficient matrix. Also the methodology developed should take advantage of this fact to minimize the number of conditions at which trial weight data need be taken. Certainly, the fact that the influence coefficients, critical speeds, and mode shapes were not found to be dependent upon torque is a confirmation of the conclusions reached by Zorzi and Nelson [4] and other [5, 6] who predicted that low (values much lower than buckling) torque levels do not alter the modes.

---

\*References are found in Section 13.0 of this report.

Denoting  $\eta_1$  as the imbalance response vector at the first torque level and  $\eta_2$  as the imbalance response vector at a second condition of axial torque, then since the influence coefficients are not torque dependent\*,

$$\eta_1 = \eta_{01} + [A] P \quad (1a)$$

$$\eta_2 = \eta_{02} + [A] P \quad (1b)$$

where  $\eta_{01}$ ,  $\eta_{02}$  vectors are the orbits prior to balancing,  $[A]$  is the influence coefficient matrix with components  $\alpha_{ij}$ , and  $P$  is the vector of correction weights. Defining a sum of squares  $S$ , where  $[W_1]$  and  $[W_2]$  are the diagonal weighting matrices as:

$$S = \bar{\eta}_1^T [W_1] \eta_1 + \bar{\eta}_2^T [W_2] \eta_2 \quad (2)$$

where

- indicates complex conjugate

T indicates matrix transpose.

Then, by an evaluation of Equation (2) and solving  $\delta S / \delta P = 0$ , the results provide a value of the correction weight set  $P$ ,

$$P = - \{ [A]^T ([W_1] + [W_2]) [A] \}^{-1} \{ [A]^T ([W_1] \eta_{01} + [W_2] \eta_{02}) \} \quad (3)$$

For the work performed herein, the weighting values for both torque conditions were assumed identical,  $[W_1] = [W_2] = [W]$ . Thus, the same importance was placed upon reducing the synchronous response of a prescribed orbit at all torque levels:

$$P = - \frac{1}{2} \{ [A]^T [W] [A] \}^{-1} \{ [A]^T [W] (\eta_{01} + \eta_{02}) \} \quad (4)$$

Equation (3) was programmed on a Digital Equipment Corp. PDP 11/34 minicomputer for laboratory balancing.

### 10.3 Program Plan

With the shaft mounted on the elastomer damper (NASA Contract NAS3-18456), the shaft was instrumented with proximity probes and the following test procedure initiated:

- The shaft was balanced in a zero torque condition
- Torque was applied to the shaft in 110 N m (1,000 in.-lb) increments to a maximum torque condition of 900 N m (8,000 in.-lb)
- The shaft was balanced using the methodology developed for all speed and torque conditions, Equation (3)

---

\*Complex vectors,  $\eta$ ,  $P$ ; Complex matrix,  $[A]$

- The synchronous measured response was compared to the predicted response
- Response was reviewed for changes in nonsynchronous motion.

**This Page Intentionally Left Blank**

## 11.0 RESULTS AND DISCUSSION

The power transmission shaft was evaluated for rotor-dynamic stability prior to testing. Analysis indicated that the rotor supported on the elastomer mount had a critical speed at 803 rpm with a logarithmic decrement calculated at 0.103. The mode shape illustrated in figure 38 indicated a simple flexural mode as the first critical speed which was confirmed by testing. During testing, the mode was located at 904 rpm with a measured logarithmic decrement of 0.129. Displacement probe locations active during testing are shown in figure 39, with the data from probes 3, 5, 6 and 8 being used for balancing data throughout this testing.

Initially the power transmission shaft was balanced conventionally so that the first bending mode could be traversed without applied torque. The center balance plane was used for this effort and for the remaining balancing. As axial torque was applied in 110 N m (1,000 in.-lb) increments, figure 40, the imbalance response through the critical increased until the critical speed could no longer be traversed without risk to the hardware. At a torque of 450 N m (4,000 in.-lb), the critical could not be traversed. This was the case as torque was increased beyond this value to a maximum value of 900 N m (8,000 in.-lb). To demonstrate the balancing methodology detailed in Equation (3), the no-torque and 900 N m (8,000 in.-lb) levels were considered as the 2 torque conditions for balancing. Baseline data obtained from the runs of figure 40 are tabulated in table 7 for the no-torque and 900 N m (8,000 in.-lb) torque conditions.

All data reported in this work was obtained using a Digital Equipment Corp. PDP 11/03 automated data acquisition system designed by MTI. The data was obtained with a speed envelope ranging from 903 to 907 rpm with the average of 10 samples computed for the data reported.

Using the balancing method developed, a predicted correction weight of 1.63 gm at an angle of  $316^\circ$  was applied to the rotor at the center balance plane. The rotor was then run under the same condition of torque loading previously noted. Figures 41 through 43 illustrate the data obtained for the probes. The predicted correction weight, when applied to the rotor, permitted traversing of the first critical speed for all torque levels. The data obtained for this balance run for the two torque levels reported in table 7 is presented in table 8 along with the predicted analytical responses.

From the data reported in tables 7 and 8, it is evident that the weighted least squares balancing approach required a tradeoff between the two torque conditions. The no-torque orbits were smaller before final balancing and the 900 N m (8,000 in.-lb) torque orbits were larger prior to the application of the correction weights; this was correctly predicted by the analysis.

If the weighting matrices,  $W_1$  and  $W_2$ , from Equation (3) are not identical, then the relative importance placed on balancing the two torque levels is not equal. Table 9 presents comparative data for this examination. Of particular significance is the result if the 900 N m (8,000 in.-lb) condition received the most importance (weighting values of unity). This correction weight (2.68 g at  $313^\circ$ ) would have caused the no-torque responses to degrade substantially. The other case of applying more significance to

the zero torque condition (0.616 g at 337°) does little to balance the 900 N-m torque condition, as expected.

One might consider an "averaging" effect by using a conventional weighted least-squares approach on the data obtained at the "average" torque level of 450 N m (4,000 in.-lb). This was performed and resulted in a predicted correction weight of 1.5096 g at 320°, close to that predicted for the correction weight used to perform this work (1.63 g at 310°). The influence coefficients used throughout this testing are provided in table 10 for reference.

## 12.0 RECOMMENDATIONS AND CONCLUSIONS

The reported balancing work is not intended to be a statement of fully developed and tested technology, but only a presentation of a basic effort which has been begun on the investigation of axial torque effects on balancing. Other testing has shown that certain modes are more susceptible to torque effects than others. Figure 44 illustrates the torque effect on the power transmission shaft for the first and third critical speeds (the second critical speed is overdamped). As shown, the third critical is more sensitive to the application of axial torque than the first mode. Therefore, it is hoped that others will investigate this effect, particularly those directly involved with power transmission shafting.

As a result of this work, the following can be concluded:

- Axial torque can substantially degrade imbalance response of long slender power transmission shafts.
- The effect of axial torque on the influence coefficients appears to be minimal. This fact can be used to reduce trial weight runs.
- A need exists for further efforts in this area to deal with multiple modes and, perhaps, modes more sensitive than reported in this work.
- Balancing at an "average torque level" might be an attractive alternative to an "averaging scheme" of equally weighting two torque conditions.

**This Page Intentionally Left Blank**



### 13.0 BIBLIOGRAPHY

1. Darlow, M.S., and Smalley, A.J., "Design and Application of a Test Rig for Supercritical Power Transmission Shafts," MTI Report 78TR41, June 1978, NASA CR-3155, 1979.
2. Darlow, M.S. and Zorzi, E.S., "Nonsynchronous Vibrations Observed in a Supercritical Power Transmission Shaft," ASME 79GT-146.
3. Tessarzik, J.M., Badgley, R.H., and Anderson, W.J., "Flexible Rotor Balancing by the Exact Point-Speed Influence Coefficient Method," J. Engr. Industry, Vol. 94, February 1972, pages 148-158.
4. Zorzi E.S. and Nelson, H.D., "The Dynamics of Rotor-Bearings Systems with Axial Torque - A Finite Element Approach," J. Mech. Design, Vol. 102, January 1980, pages 158-161.
5. Eshleman, R.L. and Eubanks, R.A., "On the Critical Speeds of a Continuous Rotor," J. Engr. Industry, Transactions ASME, Volume 91, (4B), November 1969, pages 1180-1188.
6. Galomb, M., and Rosenberg, R.M., "Critical Speeds of Uniform Shafts Under Axial Torque," Proceedings of the U.S. National Congress on Applied Mechanics, N.Y., 1961.

**This Page Intentionally Left Blank**

## FIGURES

**This Page Intentionally Left Blank**

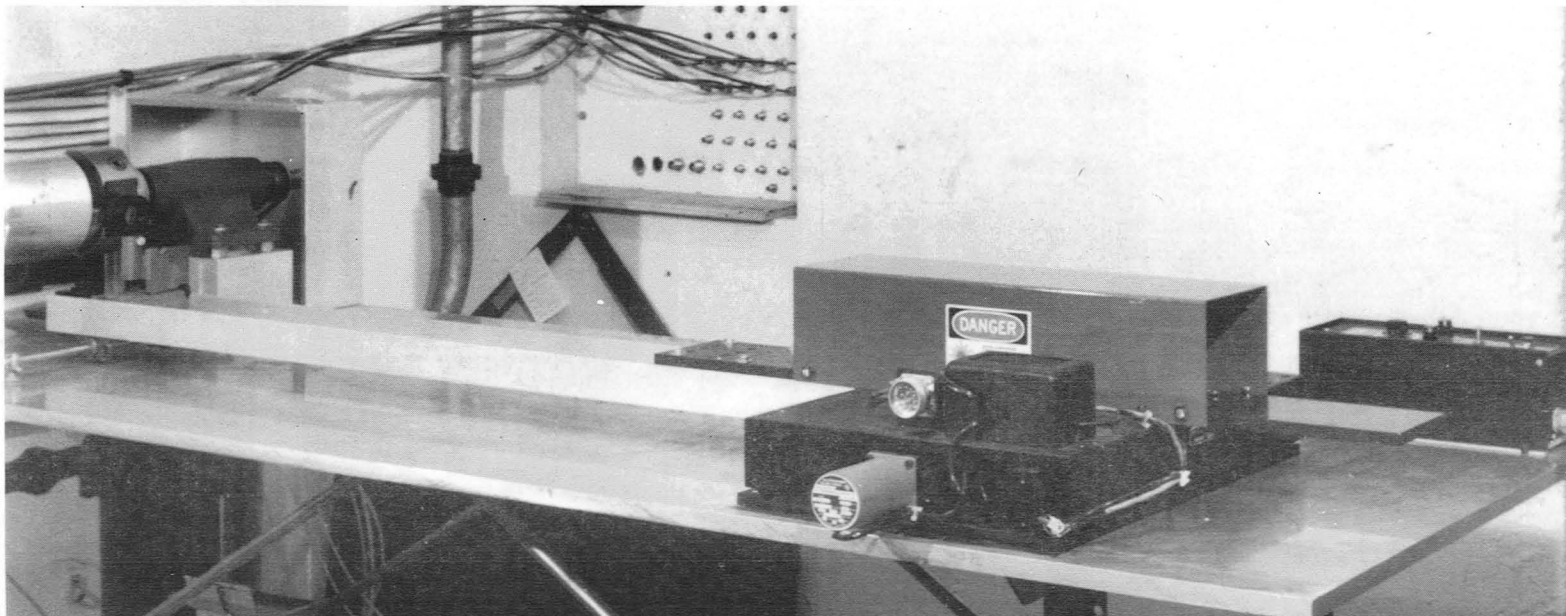


Figure 1 Specimen Test Fixture

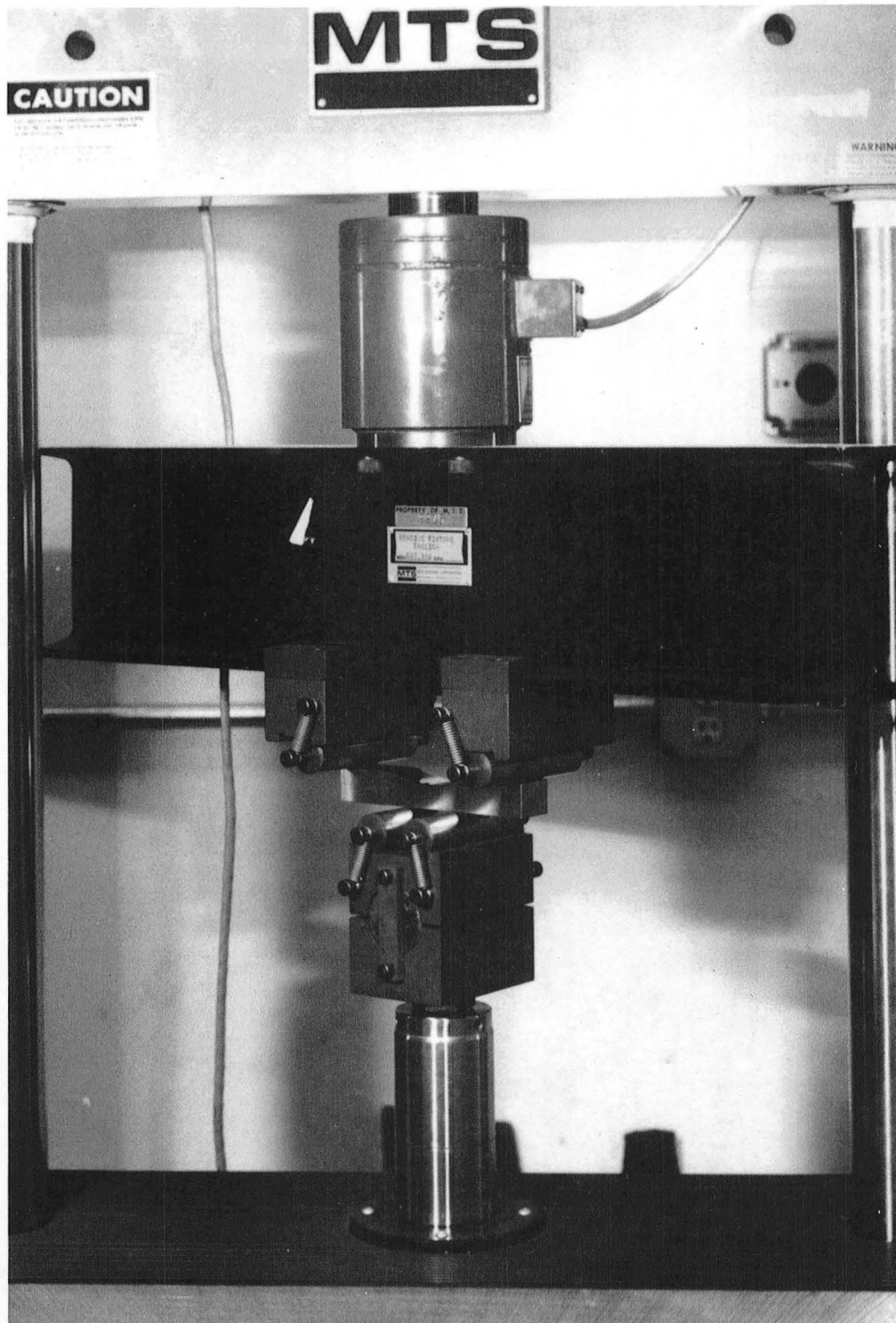


Figure 2 MTS Fatigue Machine

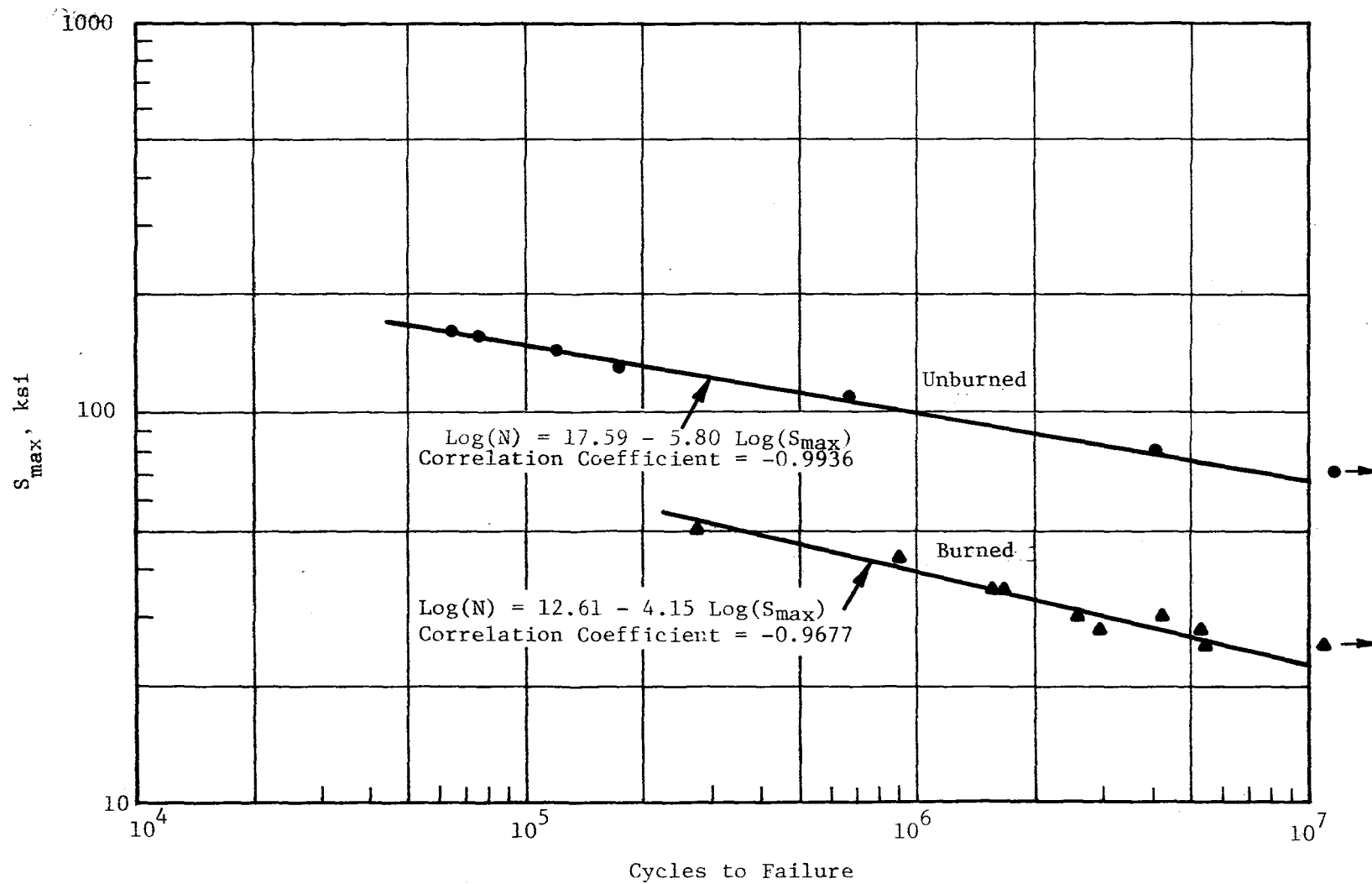


Figure 3 Inconel 718 Fatigue Data  
Stress Ratio (R) = 0.05

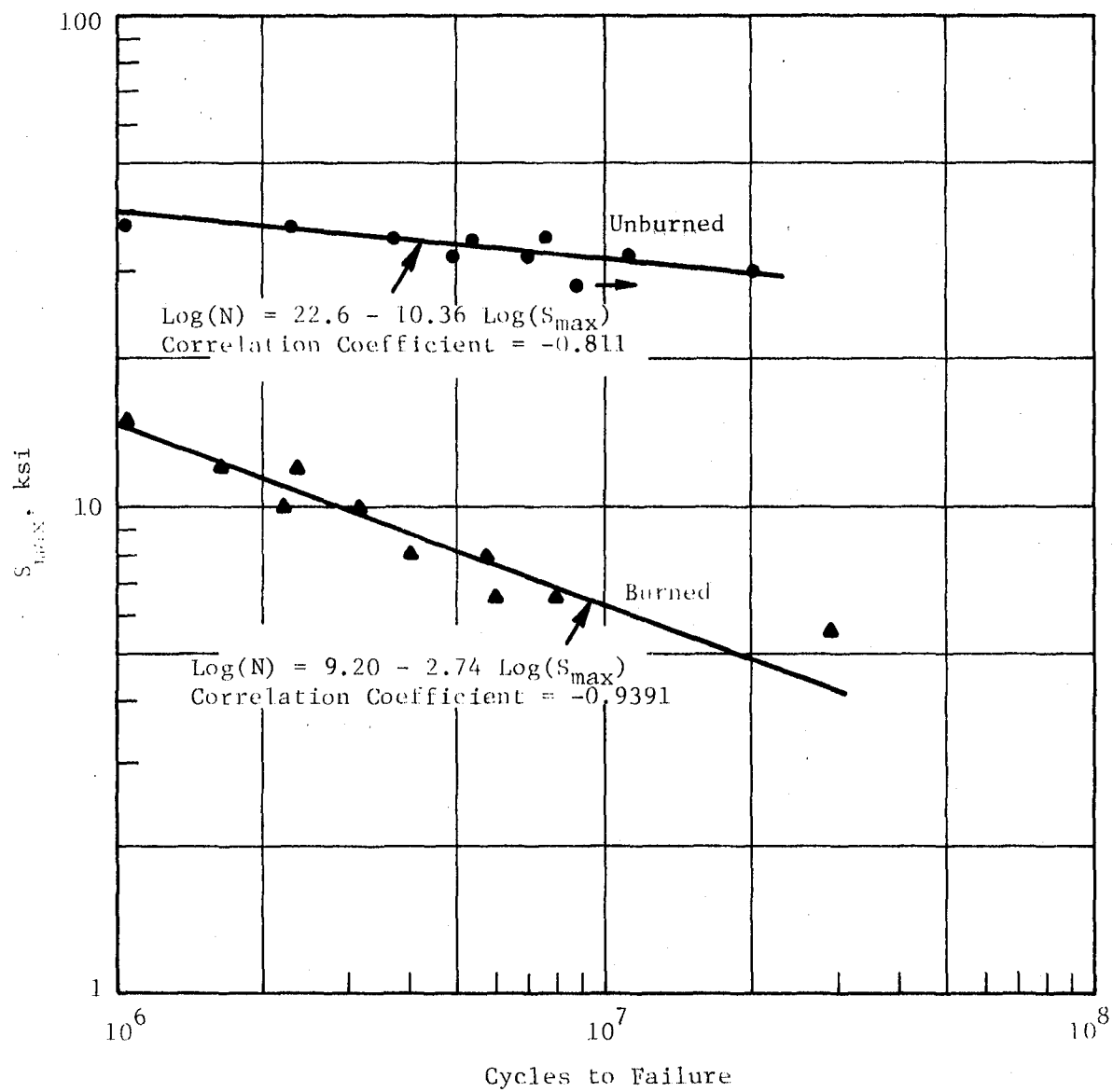


Figure 4 6061-T6 Fatigue Data  
Stress Ratio (R) = 0.05

803450



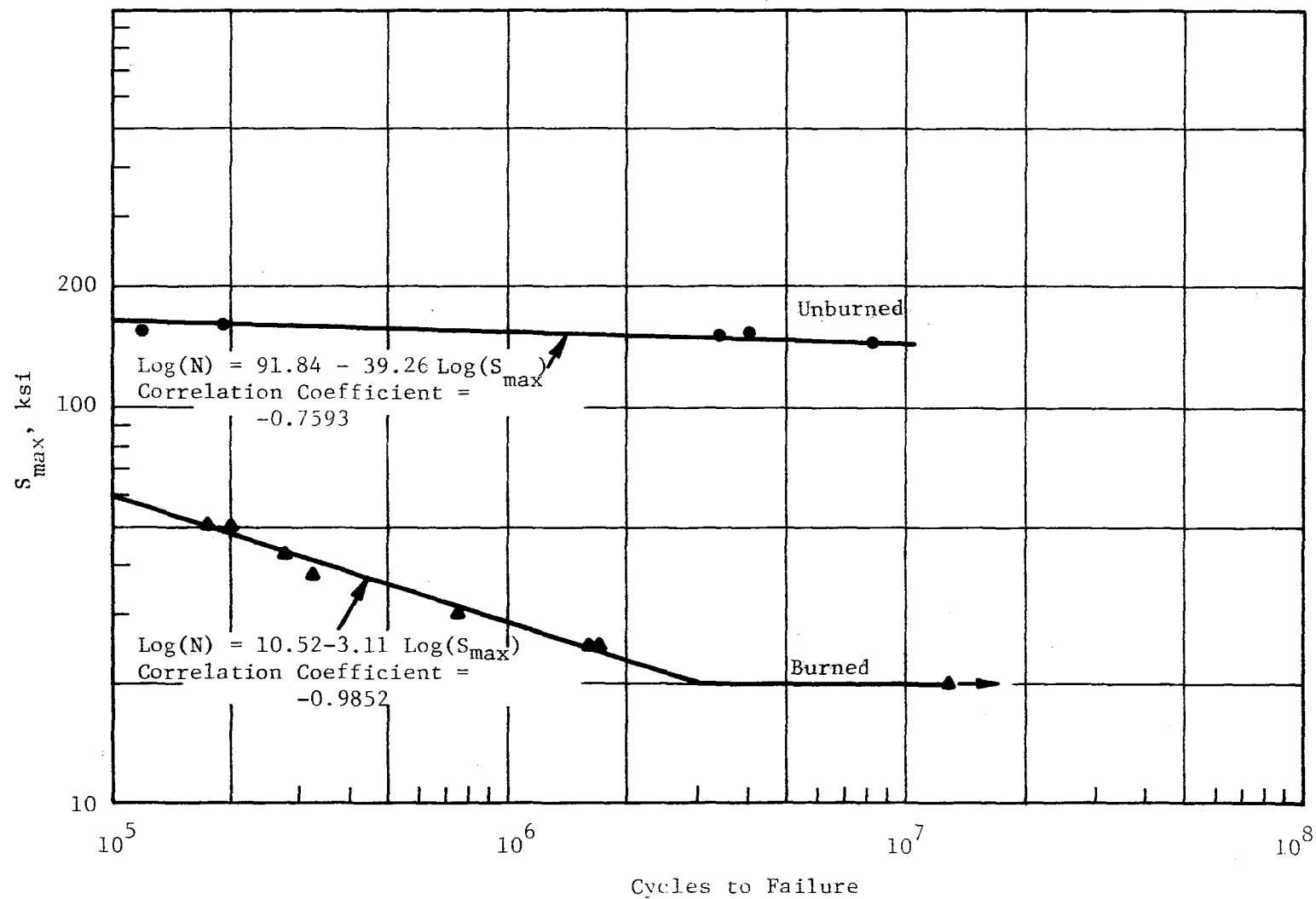


Figure 5 17-4 PH Fatigue Data  
Stress Ratio (R) = 0.05

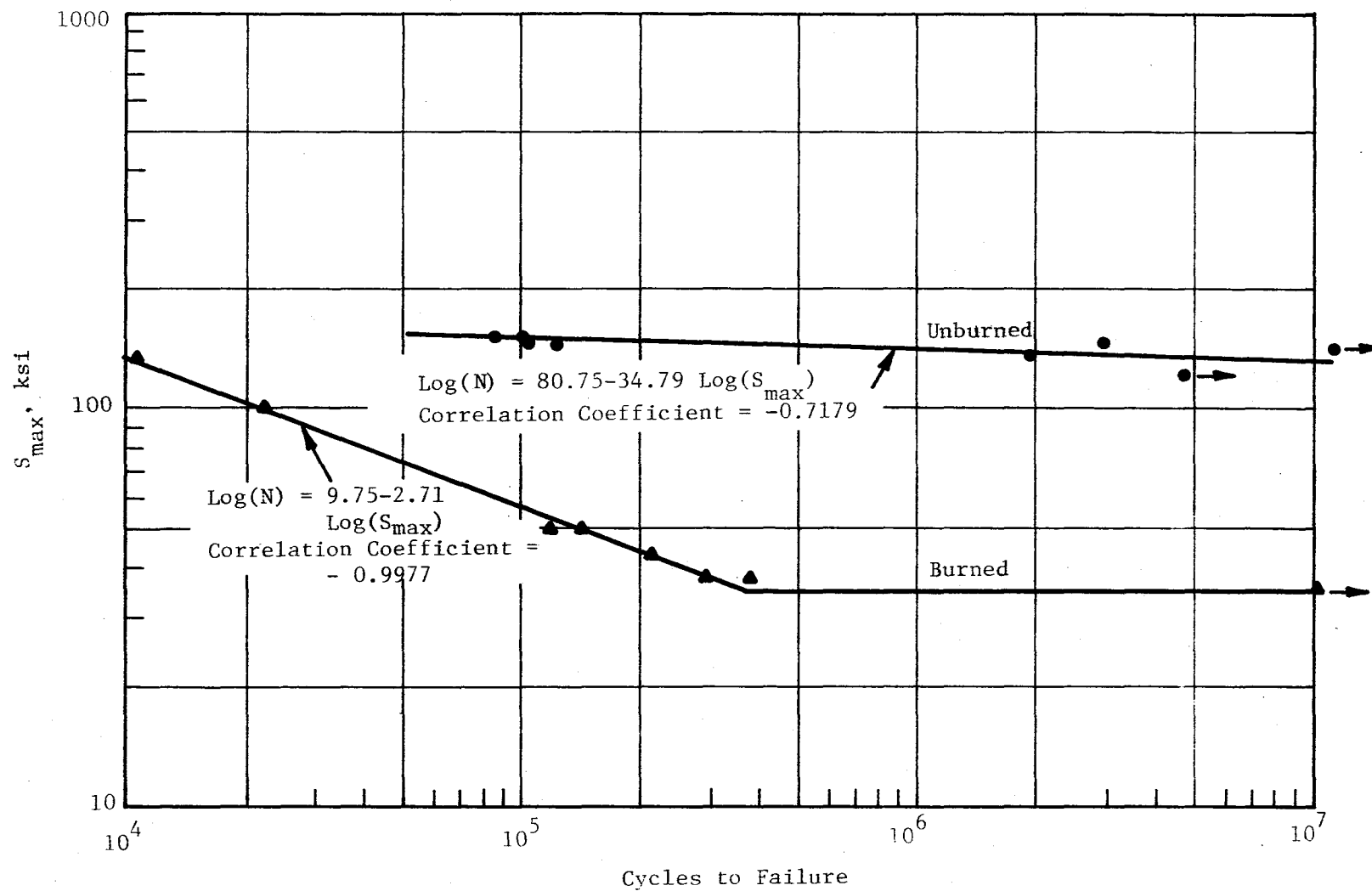
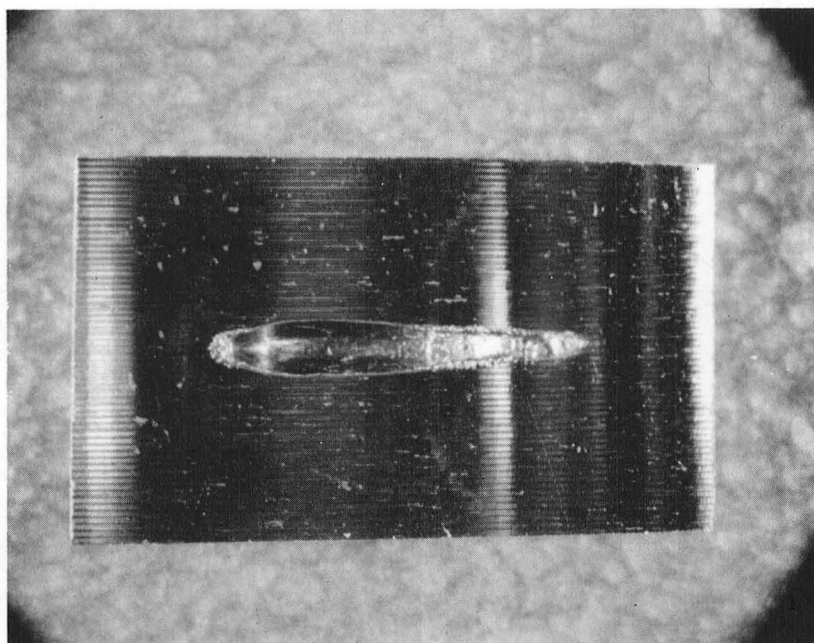


Figure 6 4340 Fatigue Data  
Stress Ratio (R) = 0.05

Beginning

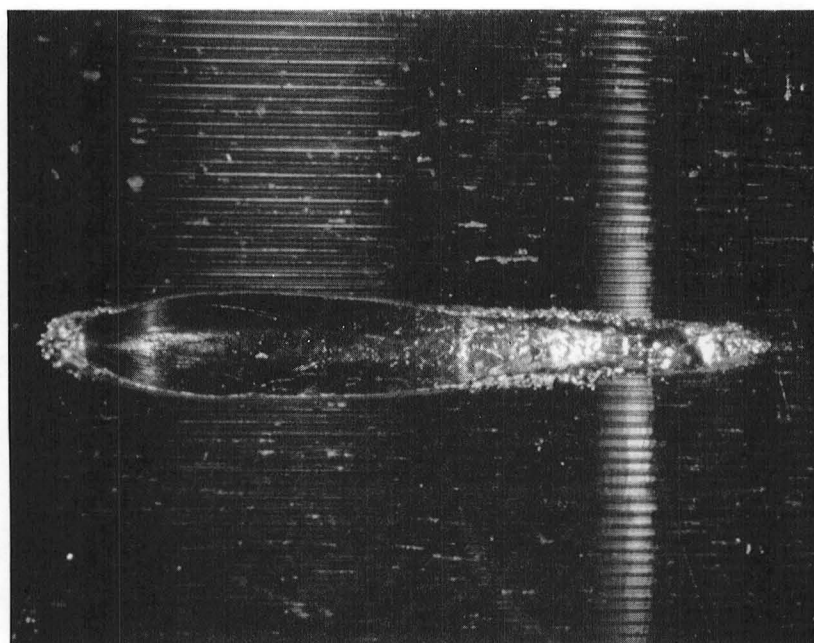


End

A. Macro photograph at 4.6X

(L1258)

Beginning



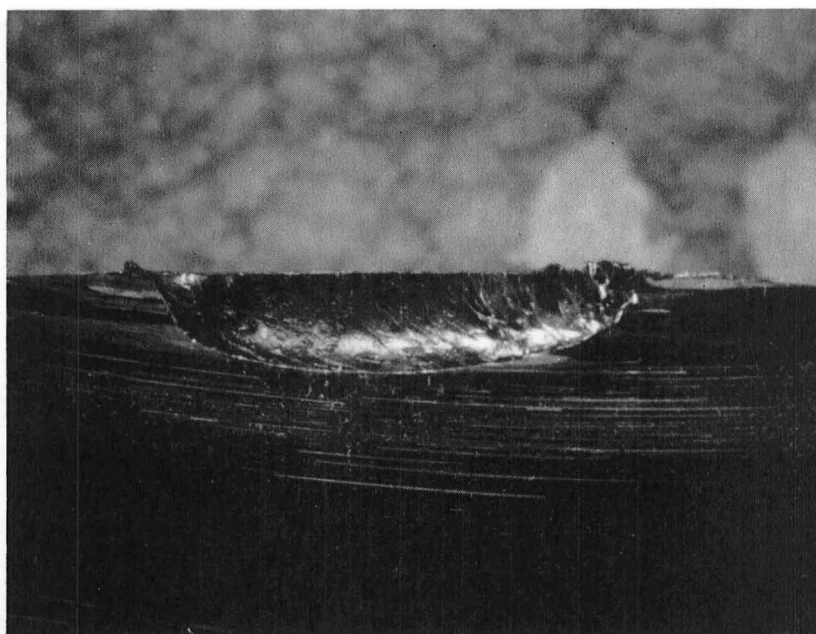
End

B. Macro photograph at 9.6X

(L1259)

Figure 7 Laser Burn in 4340 Steel: Surface Profile

Beginning

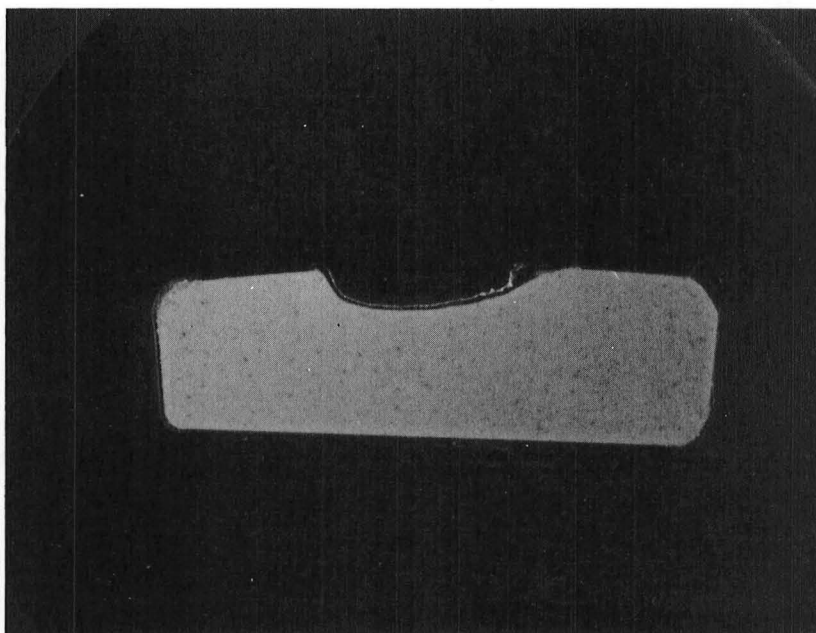


End

A. Before Mounting at 9.6X

(L1264)

Beginning



End

B. After Mounting and Metallographic  
Preparation at 4.2X

(L2205)

Figure 8 Laser Burn in 4340 Steel: Depth Profile  
Longitudinal Cross Section

↑  
End



(E1965)



Beginning

100X

(E1964)

Figure 9 Laser Burn in 4340 Steel: Surface Left in Trough  
of the Laser Burn (Scanning Electron Photomicrograph,  
Secondary Electron Image)

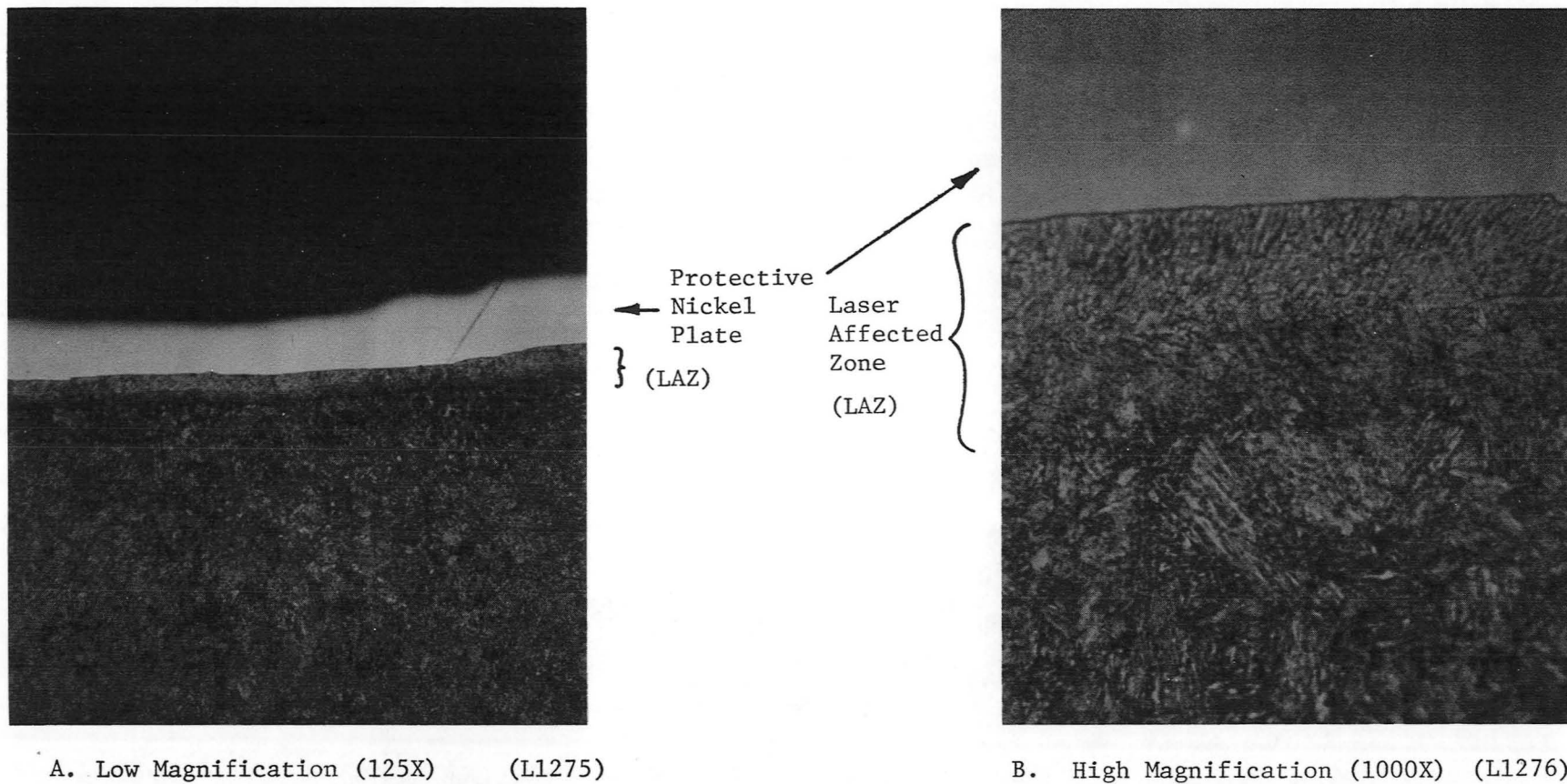
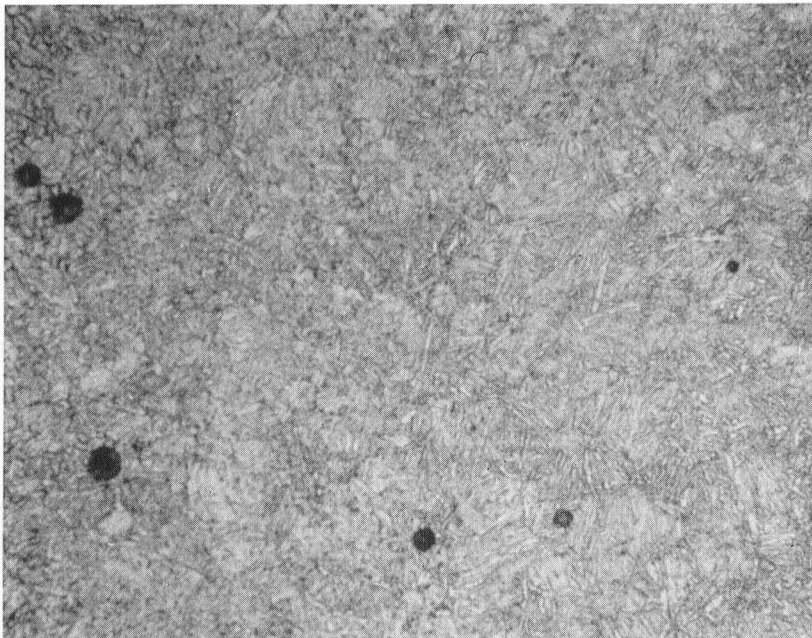
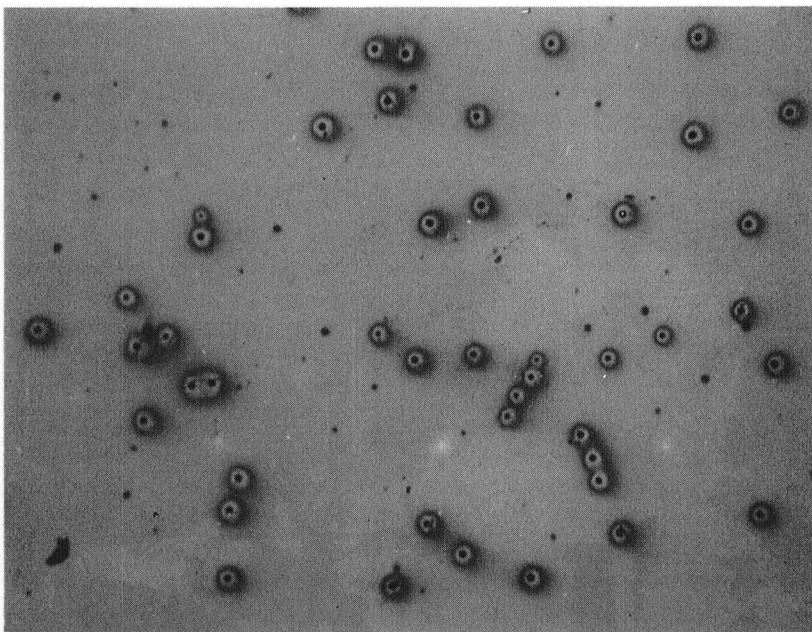


Figure 10 Microstructure of the Laser Affected Zone in 4340 Steel



A. Martensitic Microstructure and Non-metallic Inclusion at 400X (L1274)

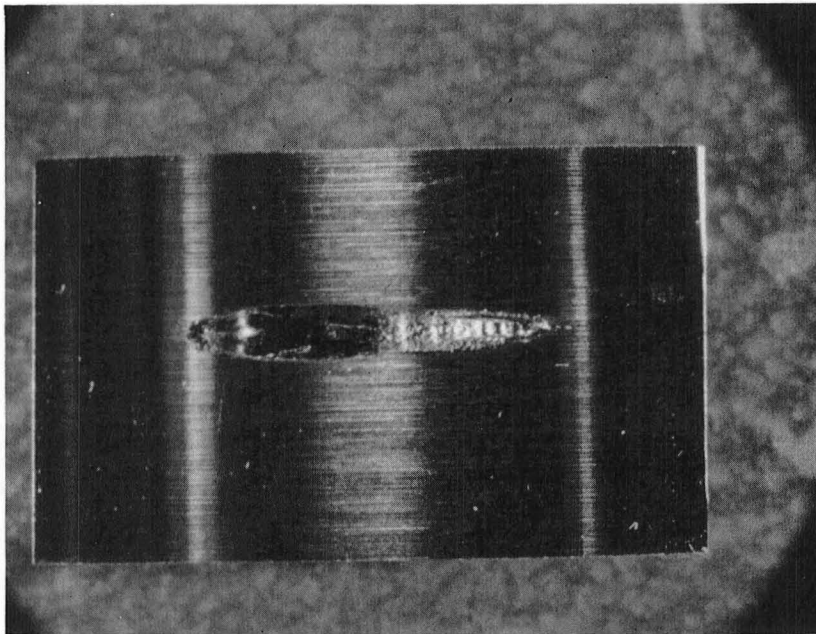


B. Nonmetallic Inclusions at 125X (L1265)

Figure 11 Bulk Microstructure of 4340 Steel (From longitudinal cross section specimen of laser burn as polished and water-rinsed to accentuate the inclusions)

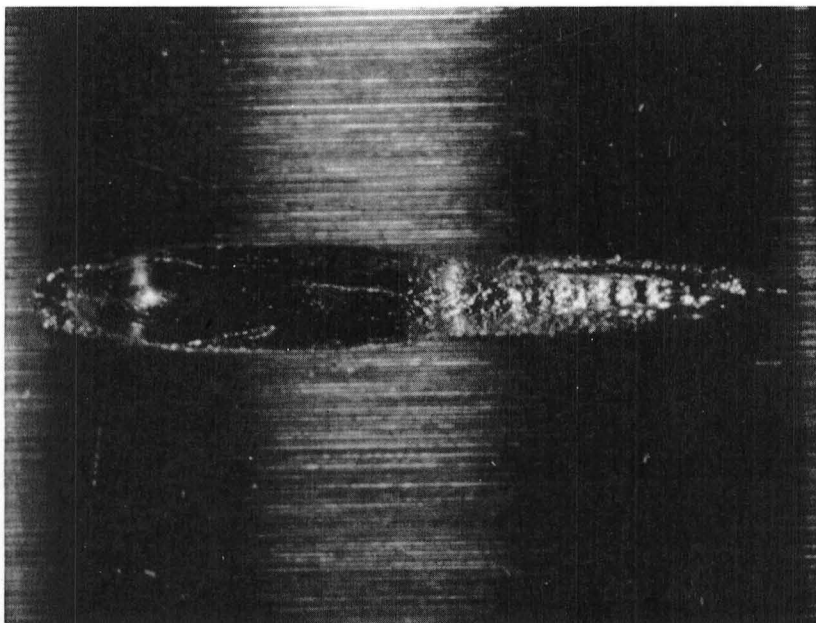


Beginning



End

Beginning



End

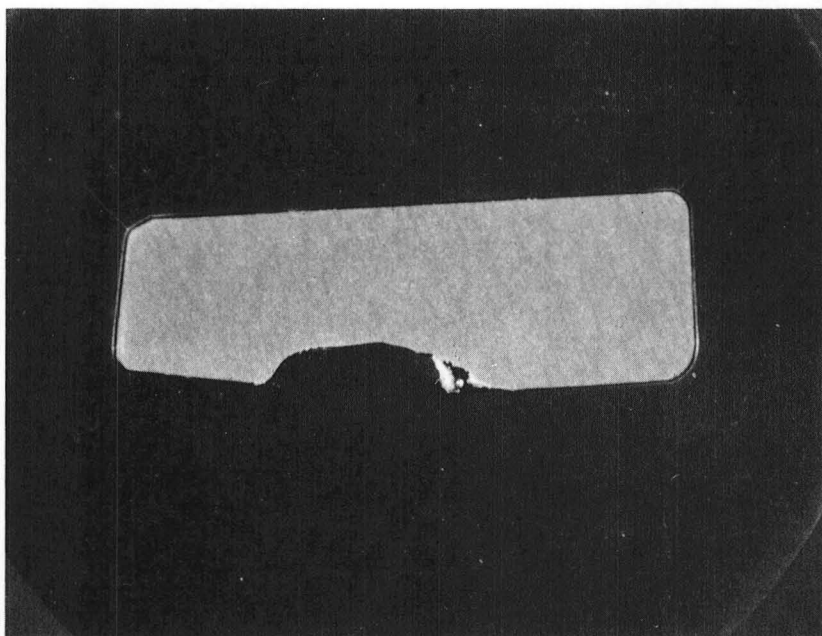
B. Macrograph at 9.6X

(L1254)

Figure 12 Laser Burn in 17-4 PH Stainless Steel:  
Surface Profile



Beginning



End

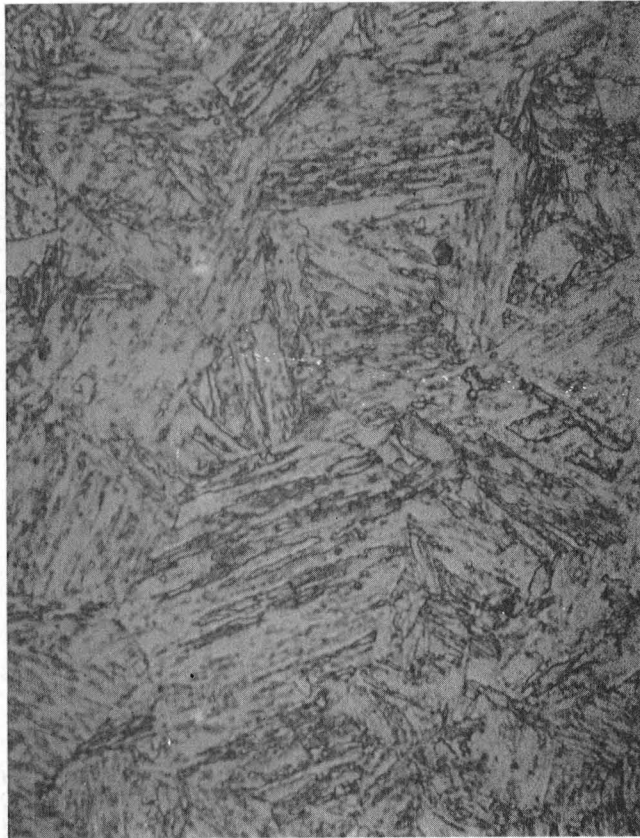
4.25X

(L2204)

Figure 13 Laser Burn in 17-4 PH Stainless Steel: Depth Profile (Metallographically Mounted and Prepared Longitudinal Cross Section)

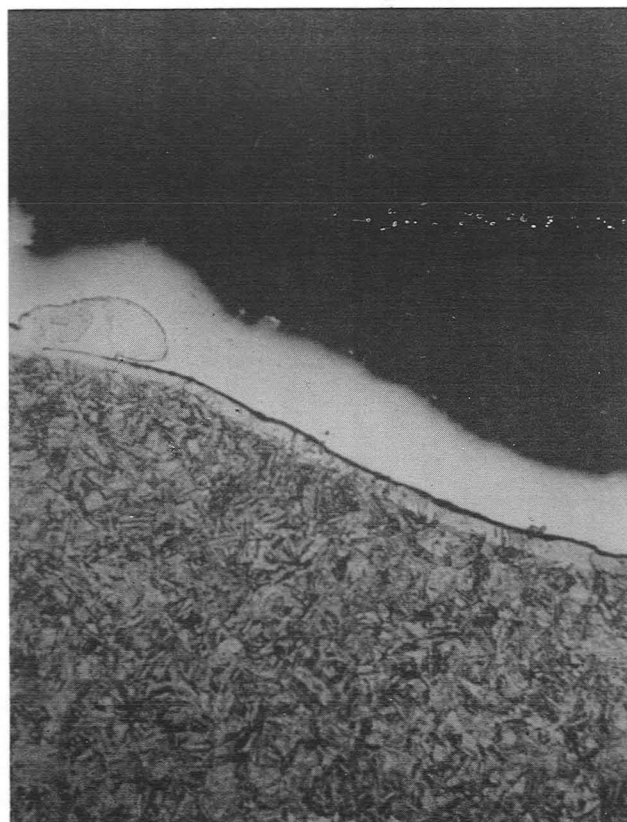


Figure 14 Laser Burn in 17-4 PH Stainless Steel: Surface Left in Trough of the Burn (Scanning Electron Photomicrographs, Secondary Electron Images)



1000X

Figure 15 Bulk Microstructure of 17-4 PH Stainless Steel (From Longitudinal Cross-Section Specimen of Laser Burn) Martensitic Structure

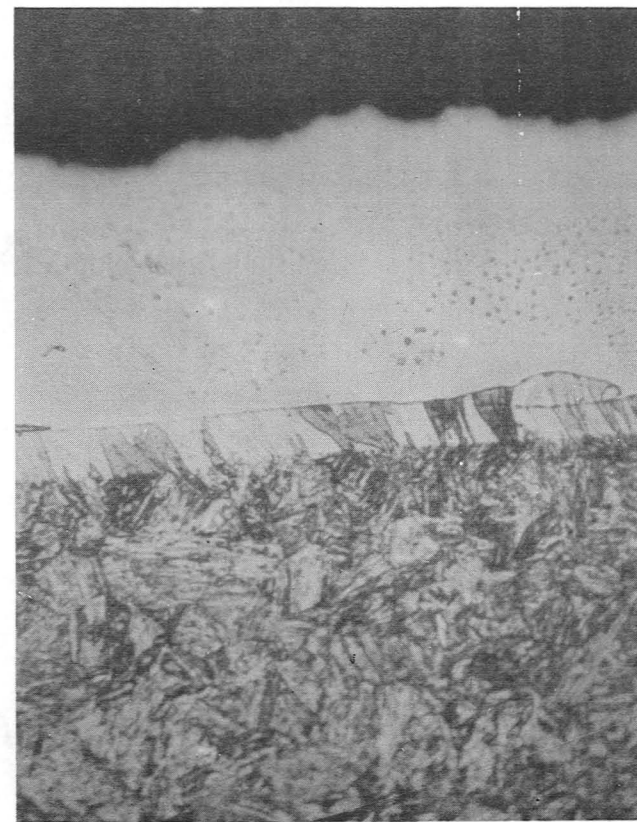


A. Midsection of Laser Burn (L1271)  
at 125X

Protective  
Nickel  
Plate

LAZ {

} LAZ



B. Midsection of Laser Burn (L1269)  
at 400X

Figure 16 Microstructure of the Laser-Affected Zone in 17-4 PH Stainless Steel  
(Directionally Solidified Martensite)



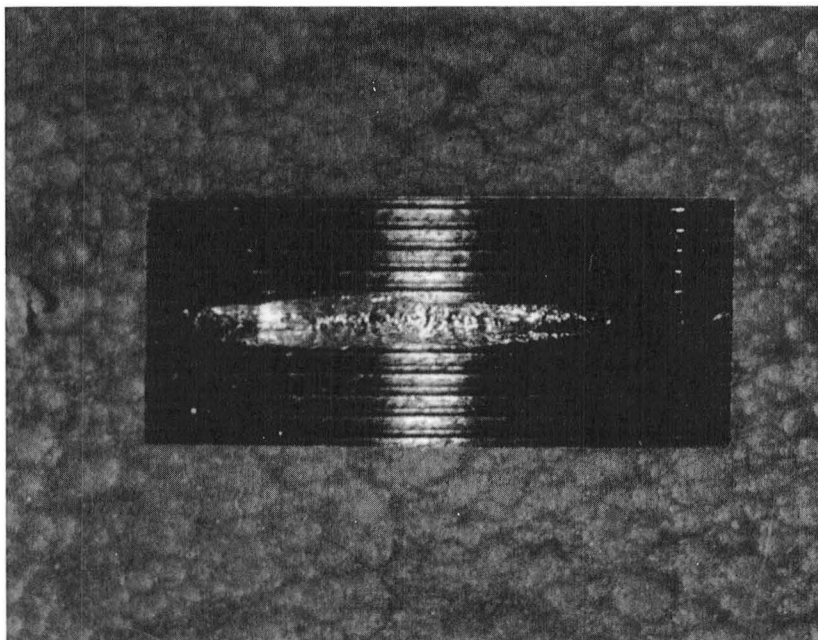
A. Very End of the Laser Burn (L1267)  
at 400X



B. Very End of the Laser Burn (L1268)  
at 1000X

Figure 17 Microstructure of the Laser Affected Zone in 17-4 PH  
Stainless Steel (Martensite-Ferrite Transformation)

Beginning

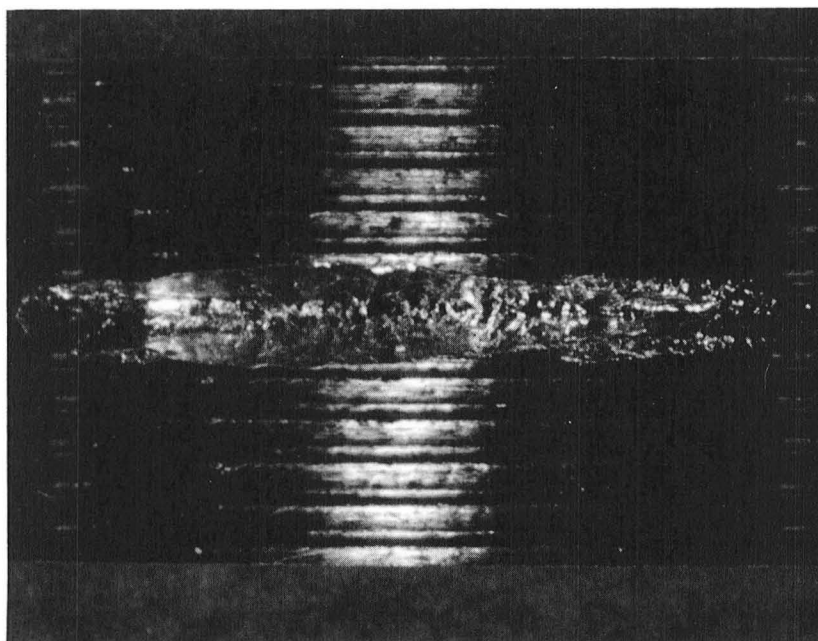


End

A. Macrograph at 4.5X

(L2181)

Beginning



End

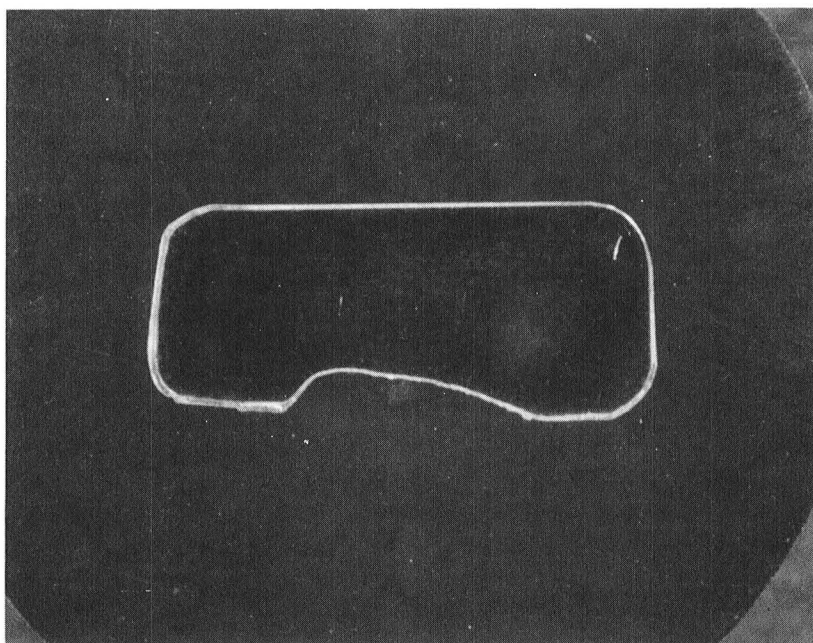
B. Macrograph at 9.2X

(L2179)

Figure 18 Laser Burn Inconel 718



Beginning



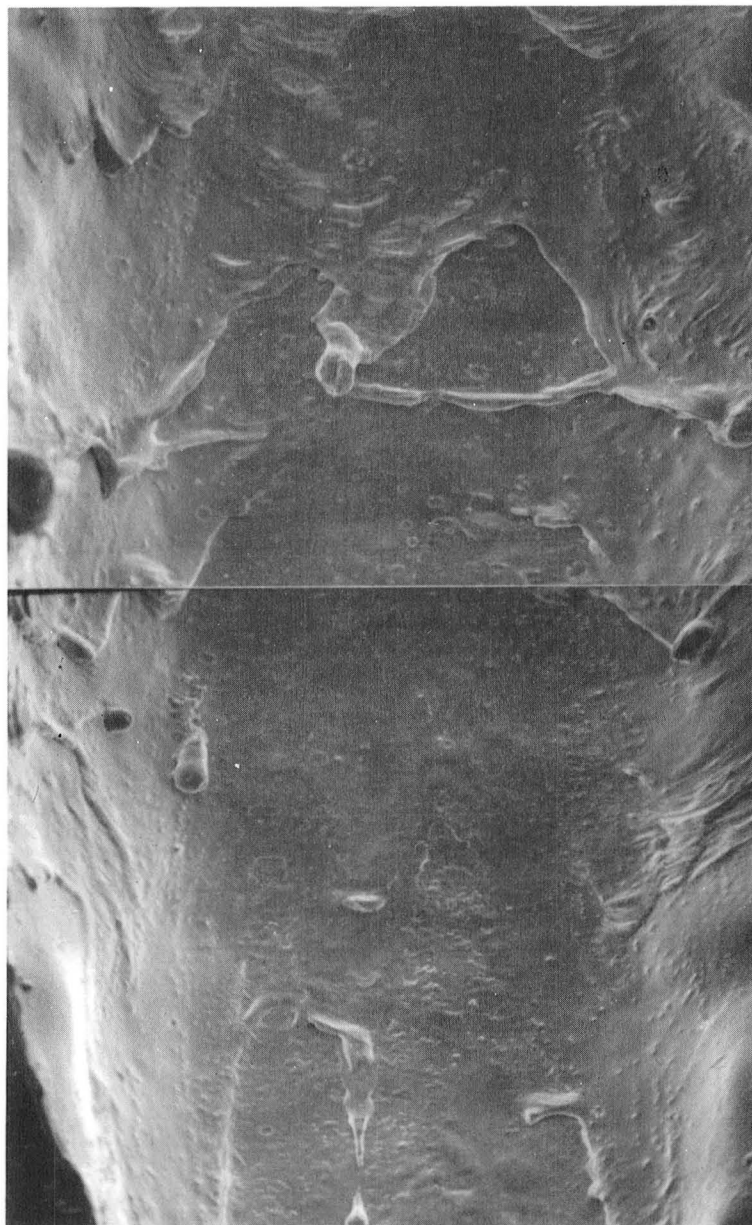
End

4.2X

(L2203)

Figure 19 Laser Burn in Inconel 718: Depth Profile (Metallographically Mounted and Prepared Longitudinal Cross Section)

↑  
End



(E2610)

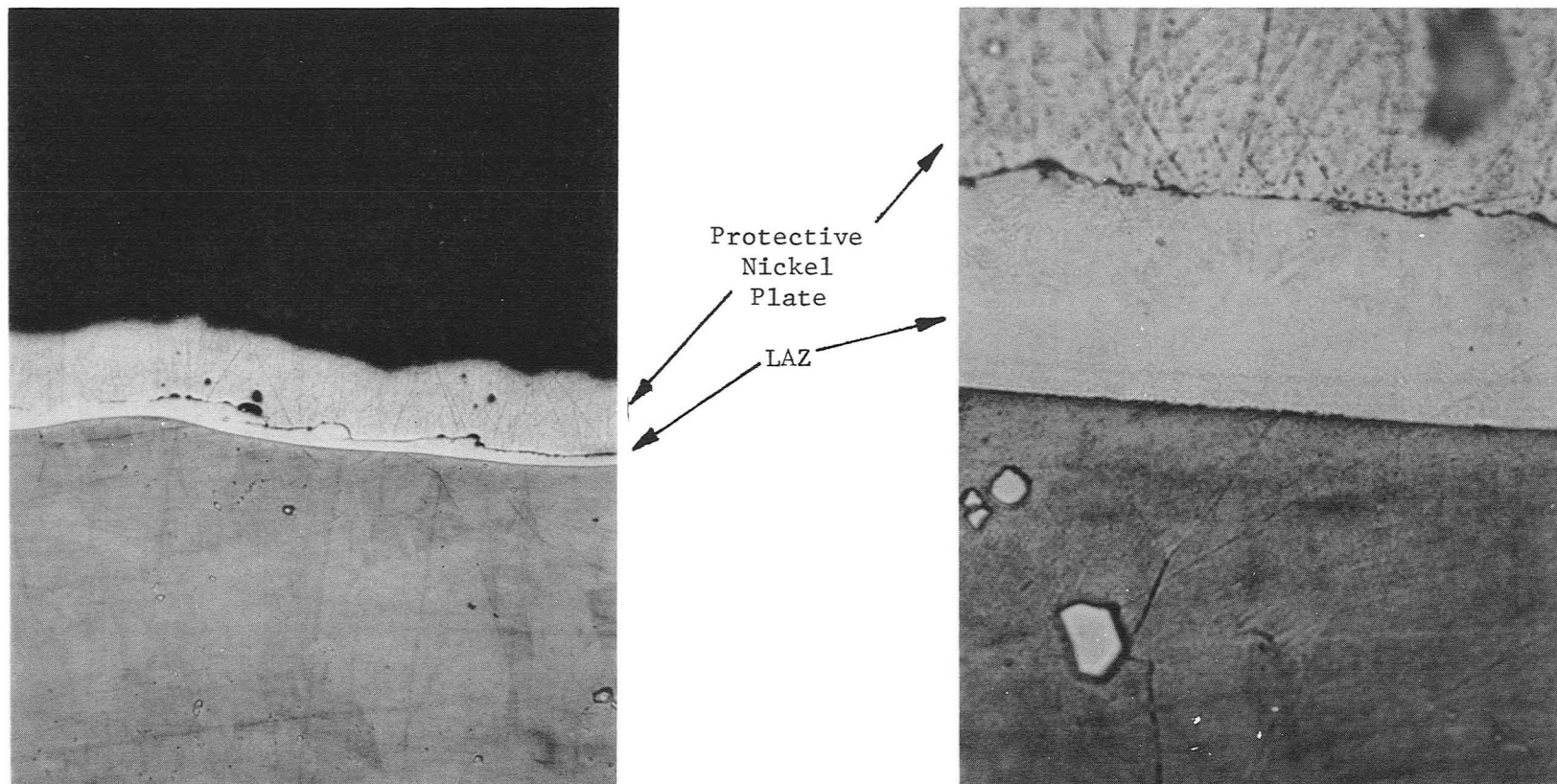
Beginning

100X

(E2609)

Figure 20 Laser Burn in Inconel 718: Surface Left in Trough of the Laser Burn (Scanning Electron Photomicrograph, Secondary Electron Image)

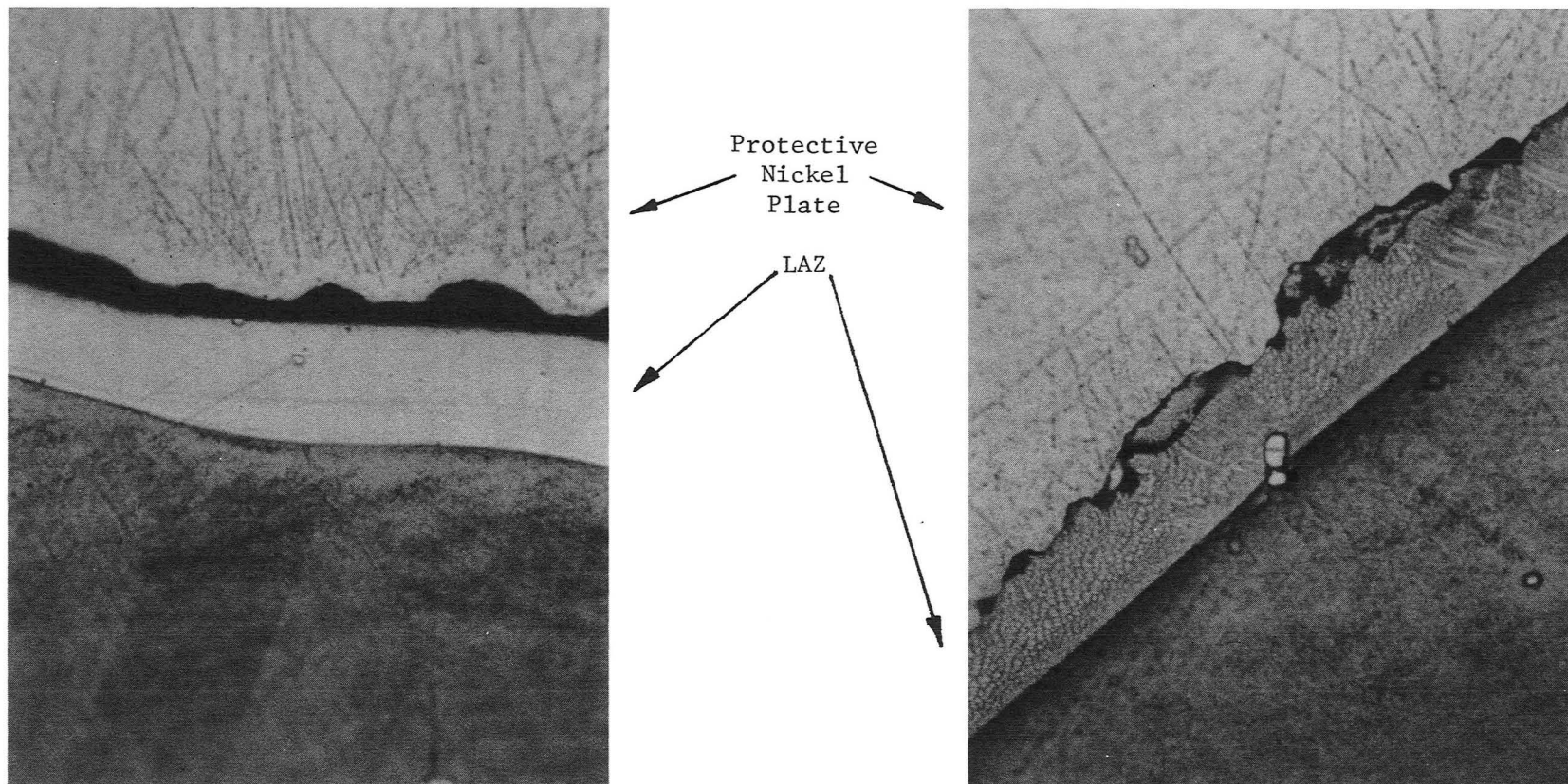




A. Midpoint of Laser Burn at 125X (L1431)

B. Midpoint of Laser Burn at 1000X (L1429)

Figure 21 Microstructure of the Laser-Affected Zone in Inconel 718 (LAZ: "As Cast" Gamma;  
Bulk: Wrought Gamma Matrix and Gamma Prime Precipitates)

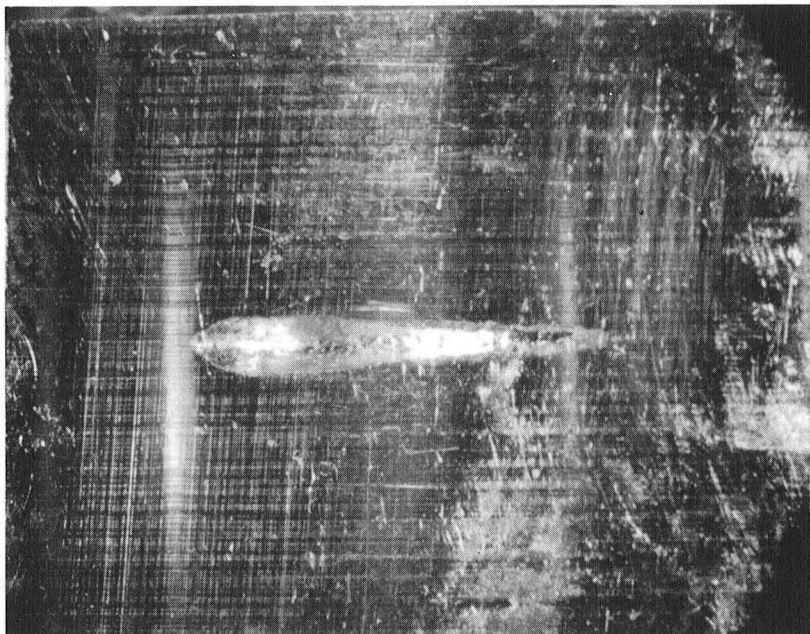


A. Near End of Laser Burn at 1000X (L1430)

B. Near End of Laser Burn at 1000X (L1428)

Figure 22 Microstructure of the Laser-Affected Zone in Inconel 718 (LAZ: "As Cast" Gamma, (Columnar Growth Evident) Incomplete Melting of Ti(C,N) Particles)

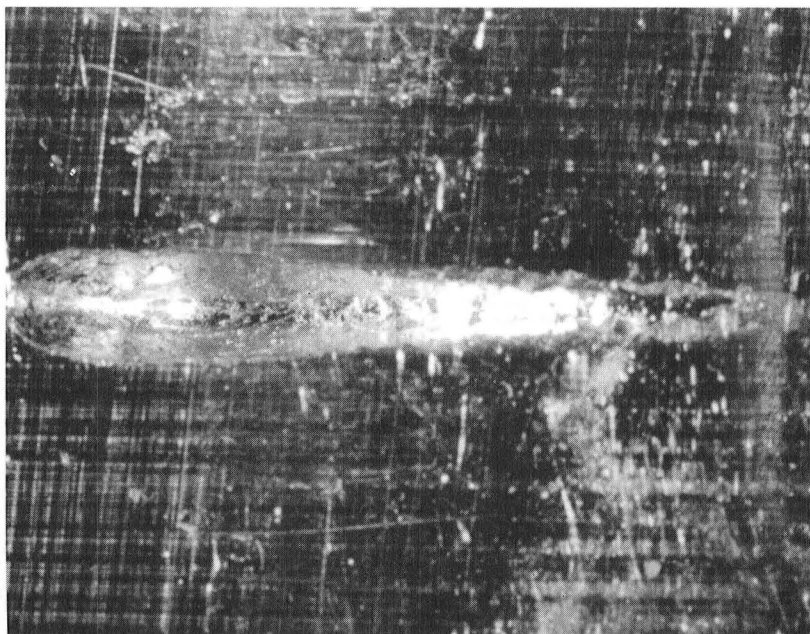
Beginning



End

A. Macro photograph at 4.64 X (L1257)

Beginning

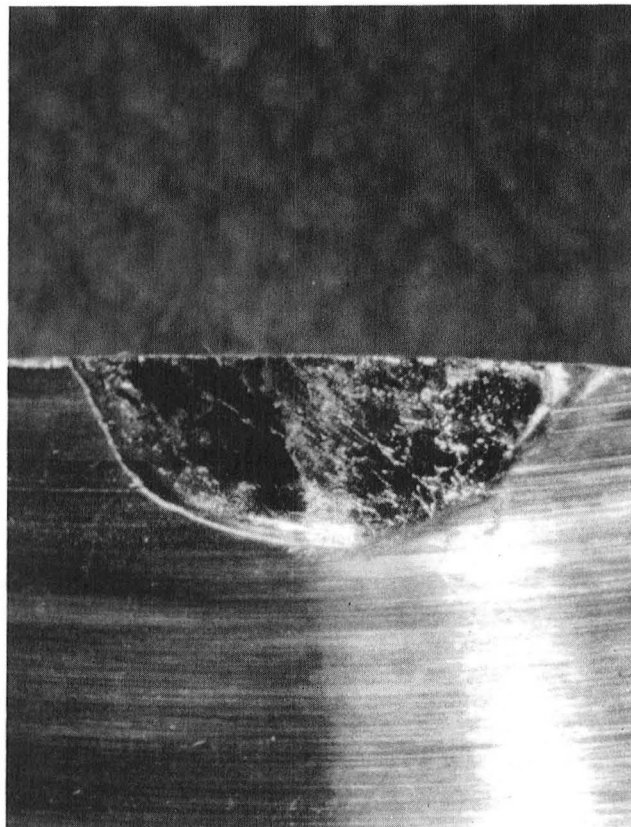


End

B. Macro photograph at 9.6X (L1258)

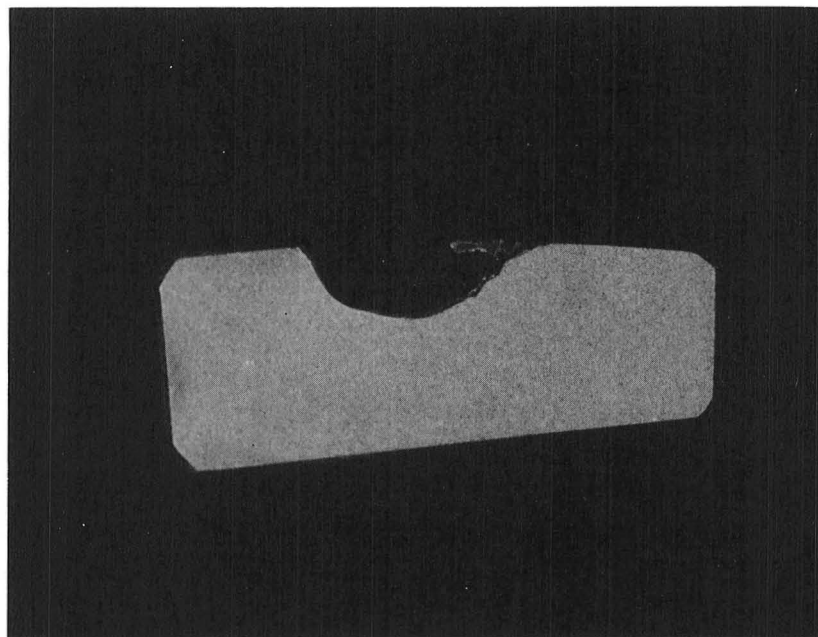
Figure 23 Laser Burn in 6061-T6 Aluminum: Surface Profile

Beginning



End

Beginning



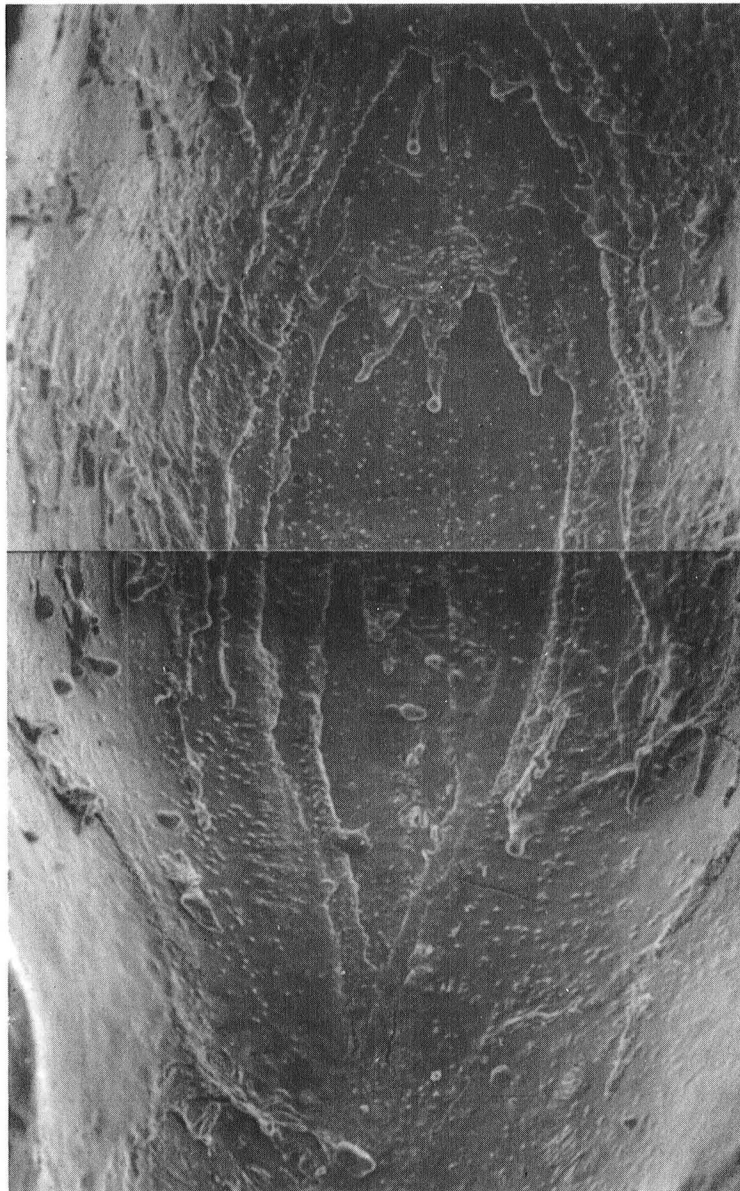
End

B. After Mounting and Metallographic Preparation at 4.25X (L2202)

Figure 24 Laser Burn in 6061-T6 Aluminum: Depth Profile  
Longitudinal Cross Section

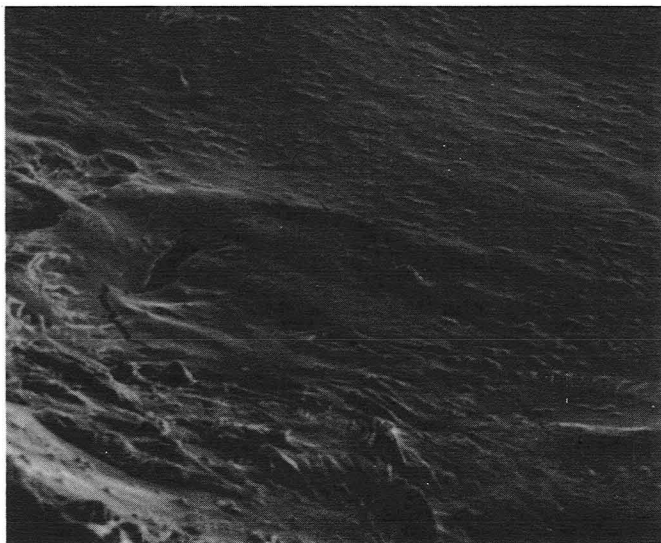


↑  
End

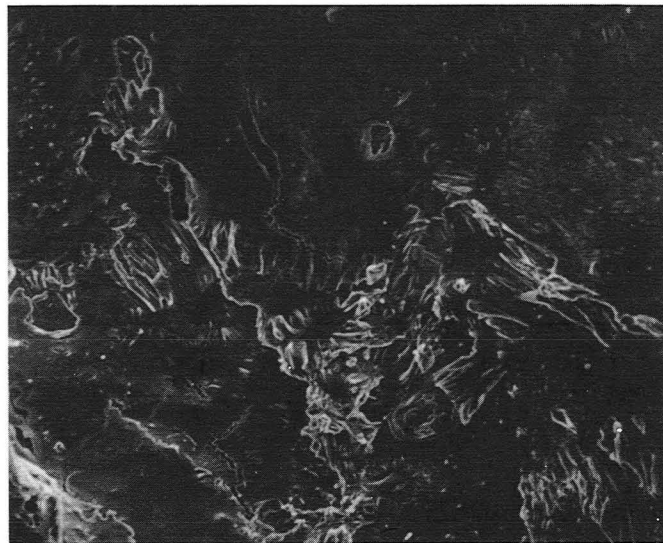


100X (E2611)

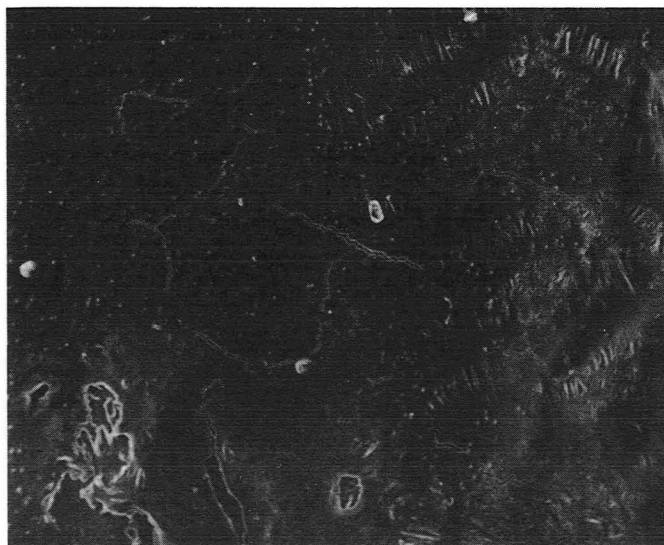
Figure 25 Laser Burn in 6061-T6 Aluminum: Surface Left in the Trough of the Laser Burn (Scanning Photomicrograph, Secondary Electron Image)



A. 150X (E1959)

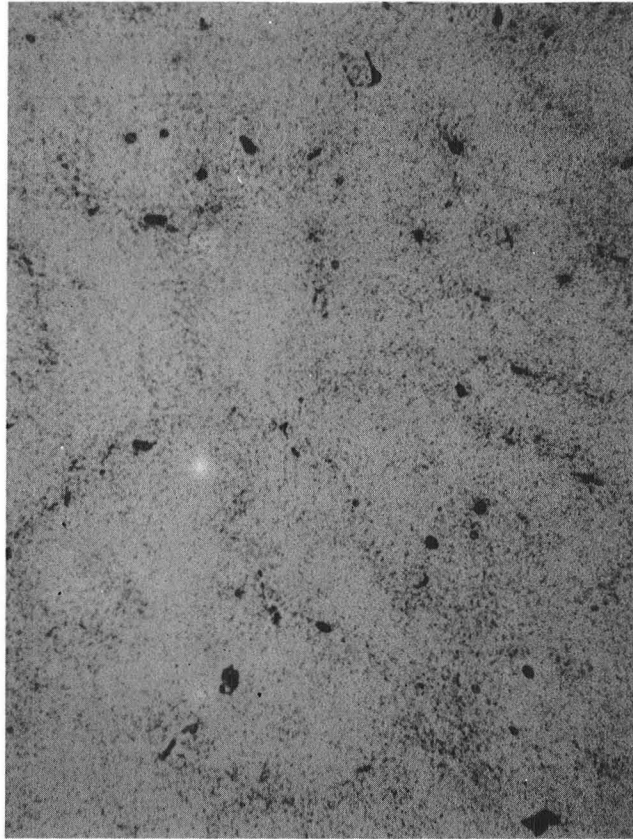


B. 100X (1960)



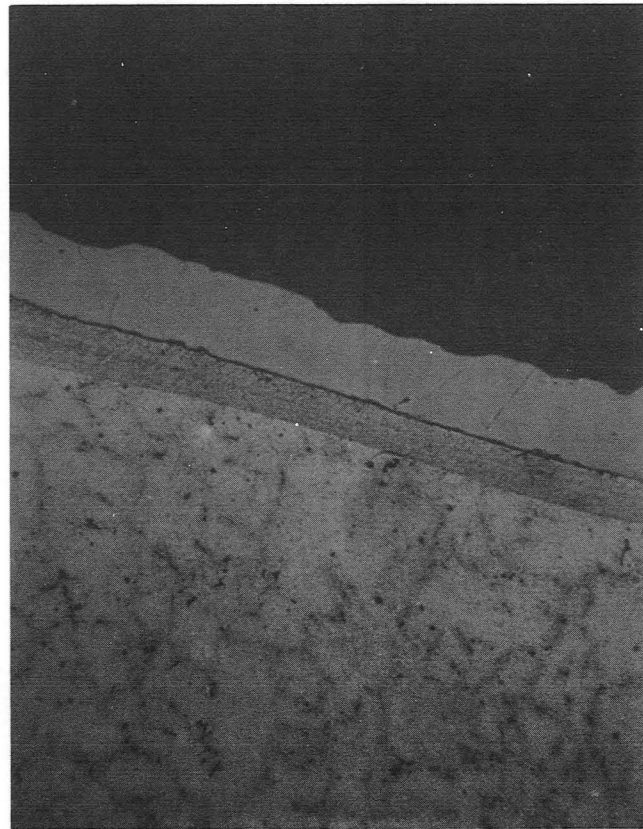
C. 100X (1961)

Figure 26 Puckering and Microcracking in 6061-T6 Aluminum Laser-Burn Surface



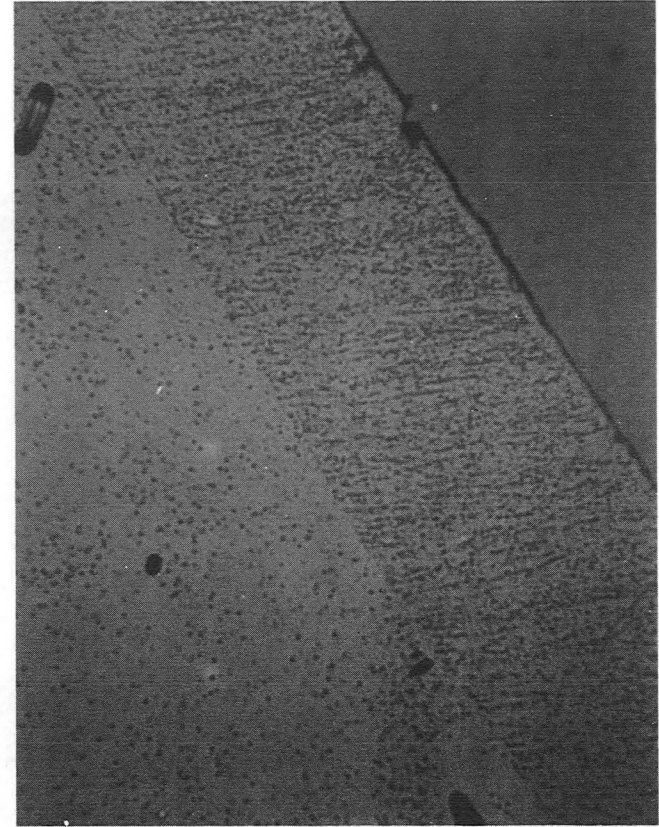
400X (L1272)

Figure 27 Bulk Microstructure of 6061-T6 Aluminum  
(From Longitudinal Cross-Section Specimen  
of Laser Burn - Mg<sub>2</sub>Si Particles (Black) and  
Fe<sub>3</sub>SiAl<sub>12</sub> Precipitates (Grey Dots) in a  
Matrix of Aluminum Solid Solution)



Protective  
Nickel  
Plate

LAZ

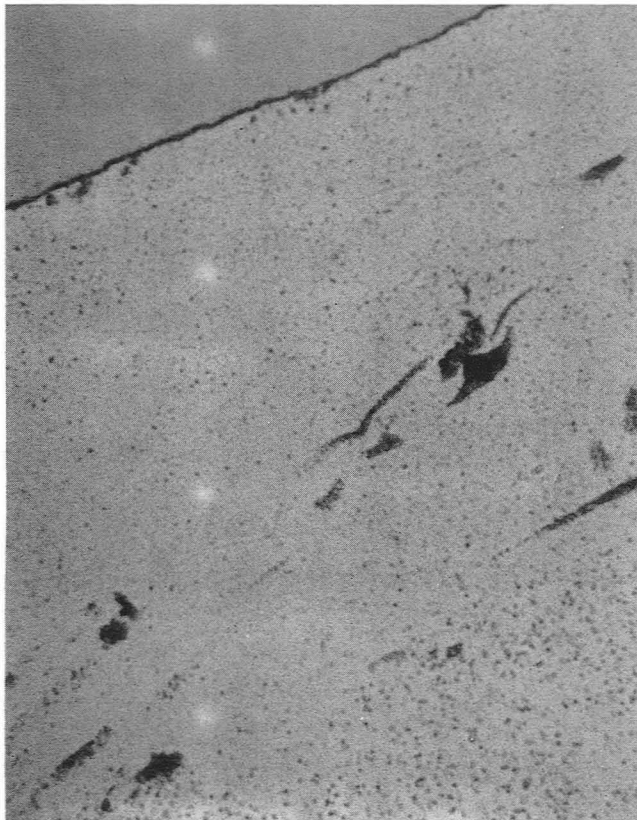


A. Magnification at 125X (L1273)

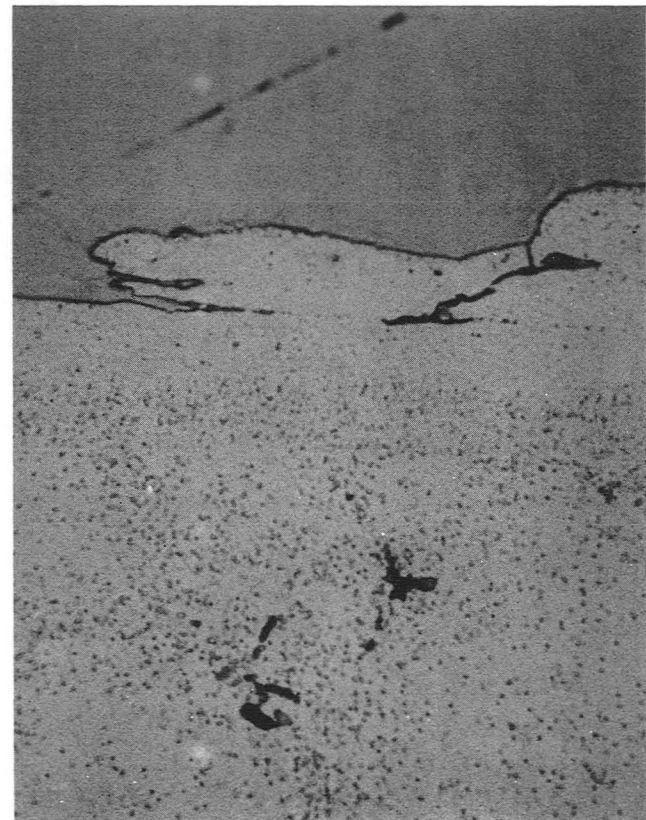
B. Magnification at 1000X (L1277)

Figure 28 Microstructure of the Laser-Affected Zone in 6061-T6 Aluminum (at the One-Quarter Distance Point Along Laser Burn) Directionally Segregated  $\text{FeSiAl}_2$  Precipitates in Matrix of Cast Aluminum Solid Solution





A. Near End of Laser Burn at 1000 X (L1279)



B. Near End of Laser Burn at 1000X (L1278)

Figure 29 Microstructure of the Laser-Affected Zone in 6061-T6 Aluminum  
 $\text{FeSiAl}_{12}$  Precipitates in a Cast Aluminum Solid Solution Matrix

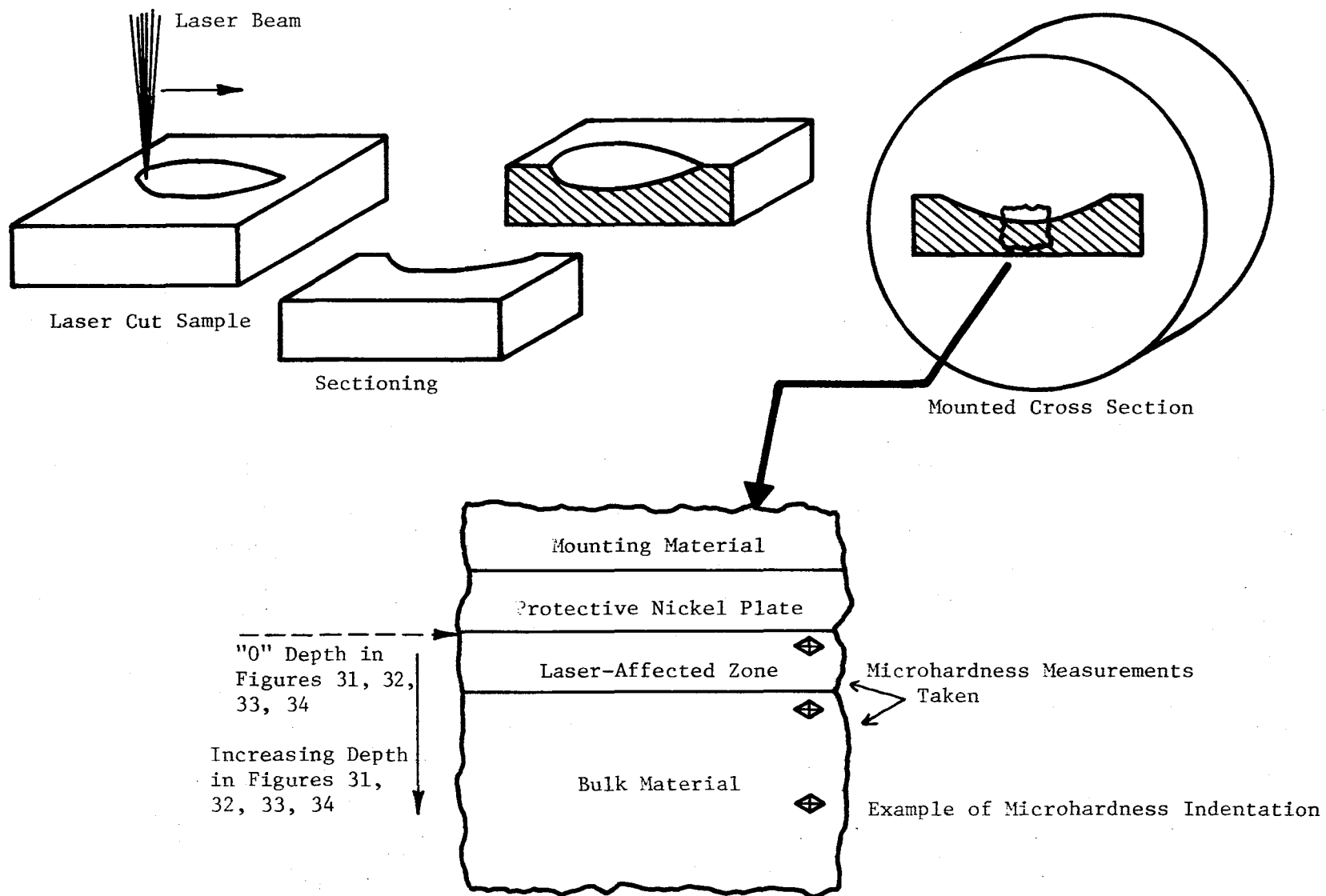


Figure 30 Sketches of Laser Cut Sample: Sectioning, Mounting and Microhardness Measurements

Laser-Affected Zone ( $\sim 32 \mu\text{m}$ ) 1.26 mil (determined microscopically)

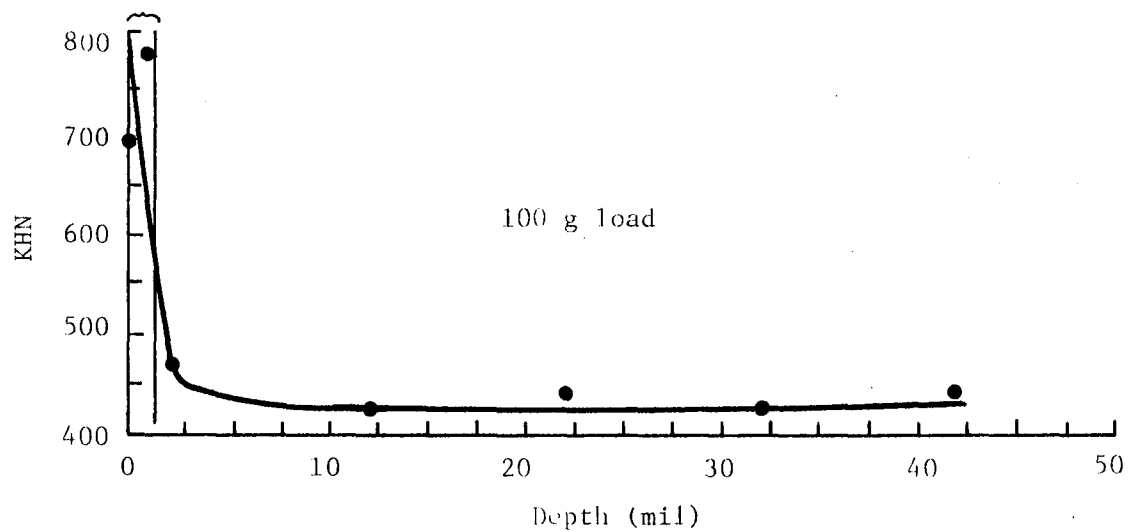


Figure 31 Microhardness - Depth Profile: 4340

803448

Laser-Affected Zone ( $\sim 40 \mu\text{m}$ ) 1.57 mil (determined microscopically)

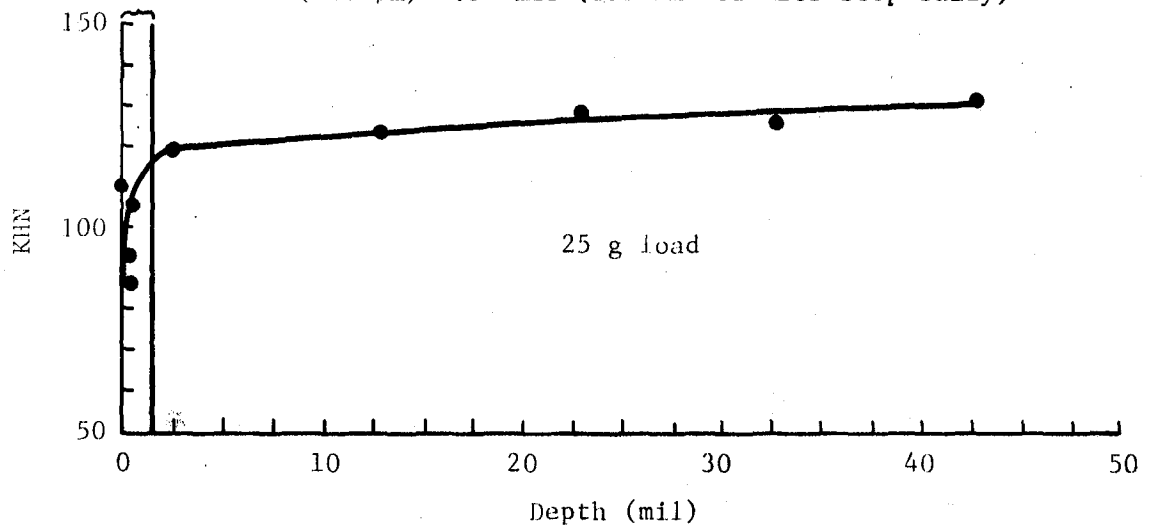


Figure 32 Microhardness - Depth Profile: 6061-T6

803442

Laser-Affected Zone ( $\sim 18 \mu\text{m}$ ) 0.71 mil (determined microscopically)

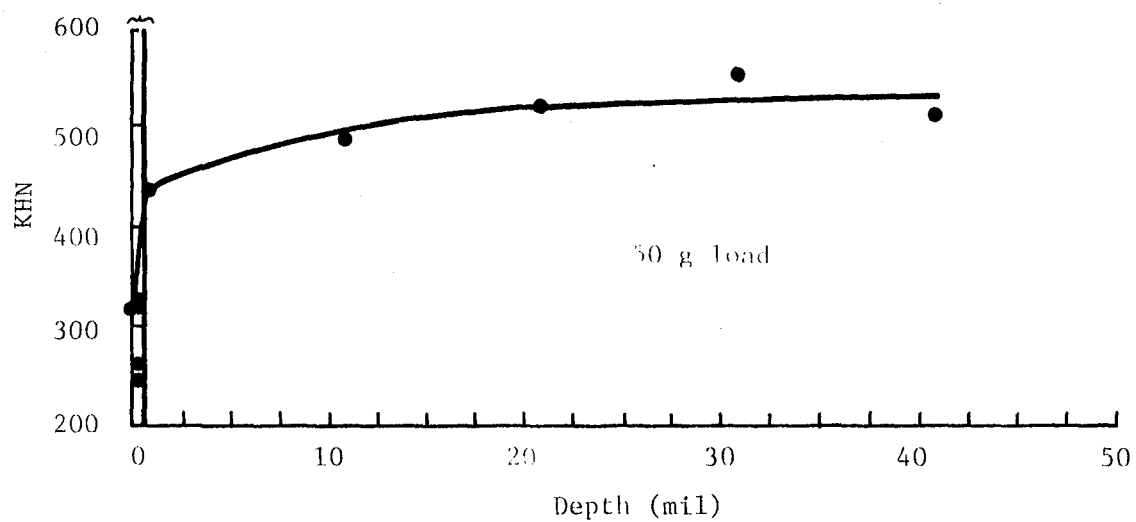


Figure 33 Microhardness - Depth Profile: 17-4 PH

803441

Laser-Affected Zone ( $\approx 18 \mu\text{m}$ ) 0.71 mil (determined microscopically)

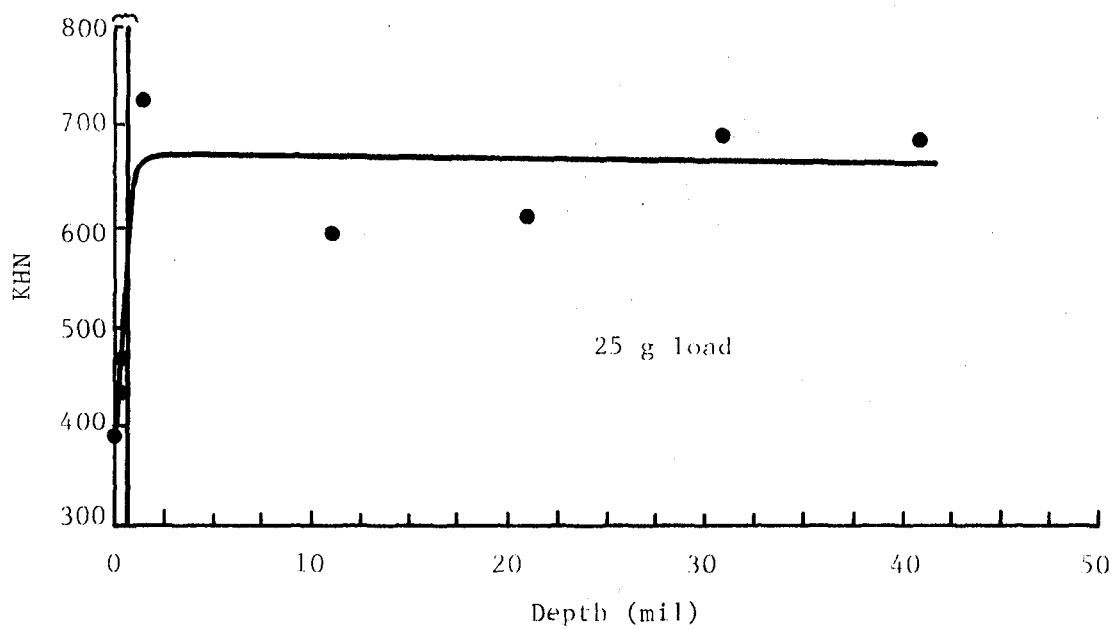


Figure 34 Microhardness - Depth Profile: Inconel 718

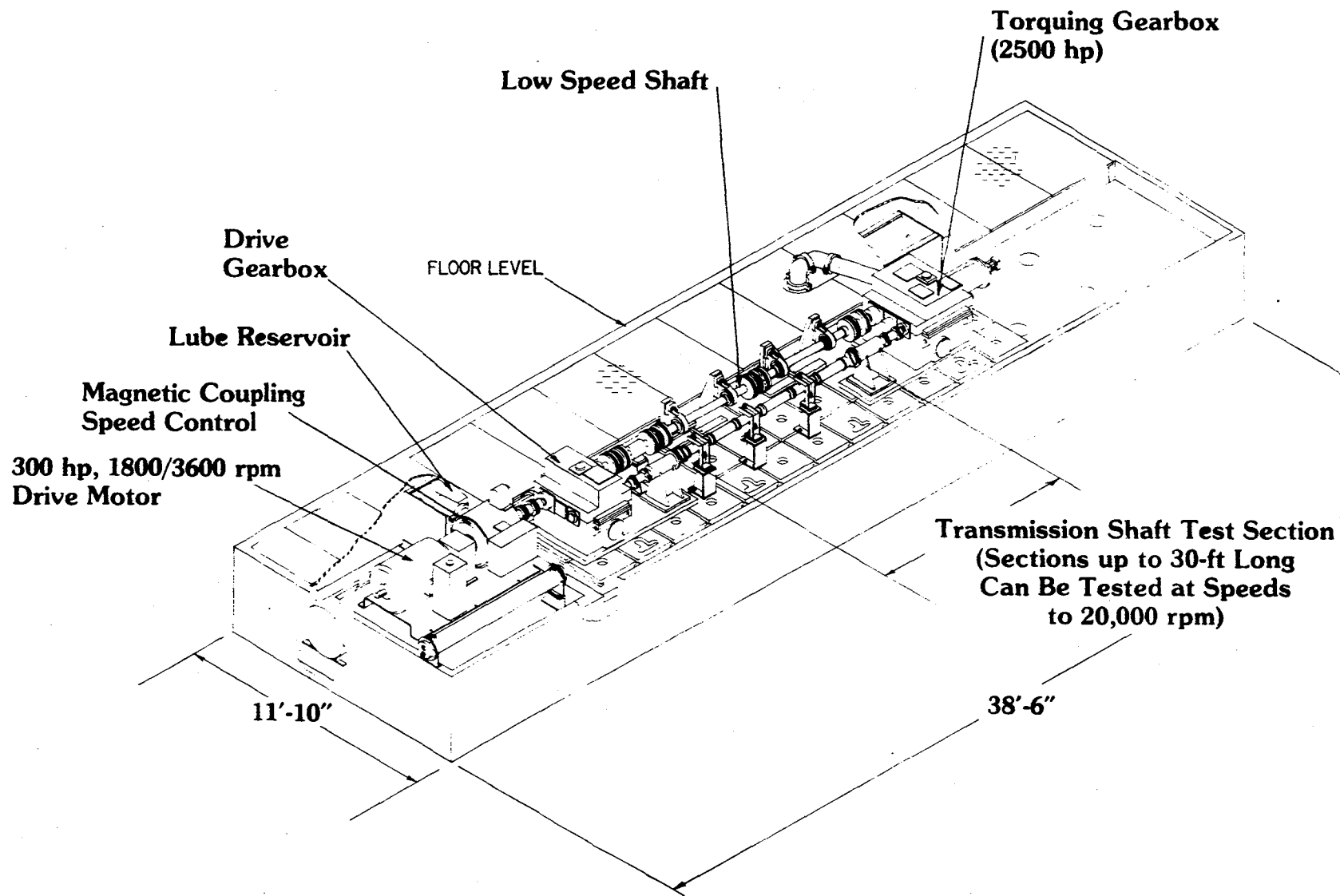


Figure 35 Drive Train Dynamics Technology Test Rig Configuration for High-Speed Shaft Balancing

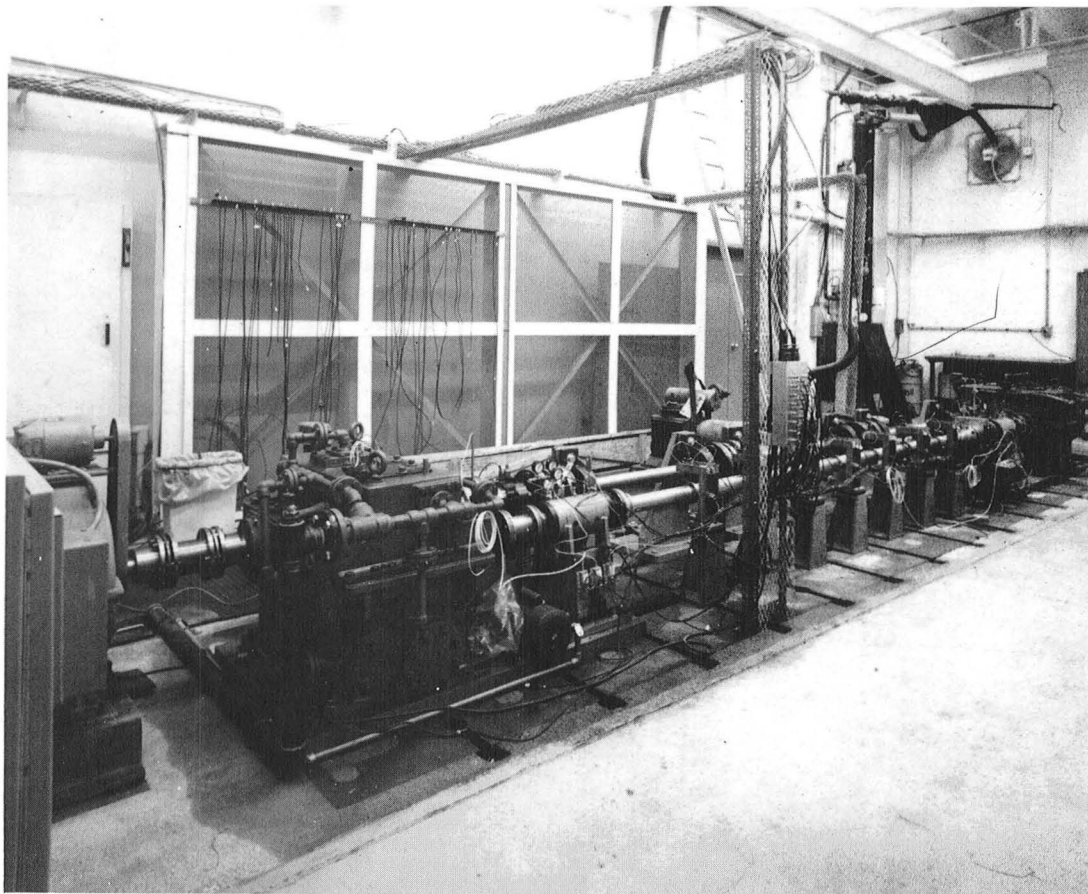
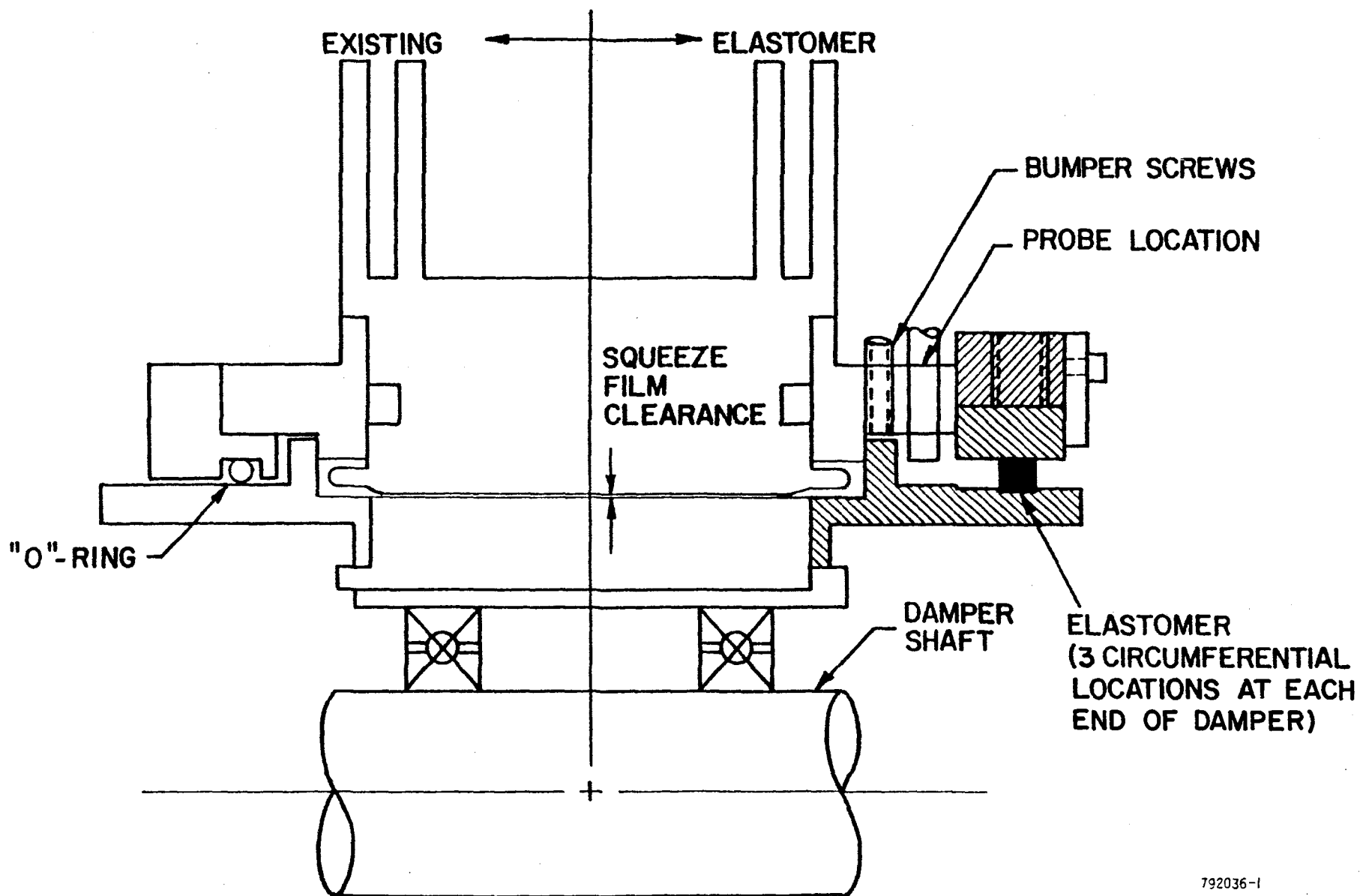


Figure 36 . View of Completely Assembled Test Rig Showing  
High-Speed Side from Drive Gearbox End





792036-1

Figure 37 Elastomer Damper/Squeeze-Film Damper Schematic

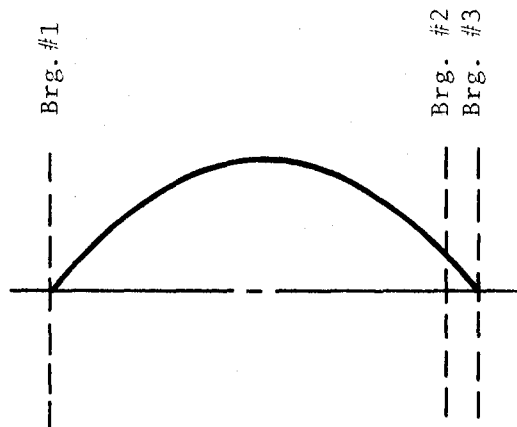


Figure 38 First Rotor Critical Speed Mode Shape

803453

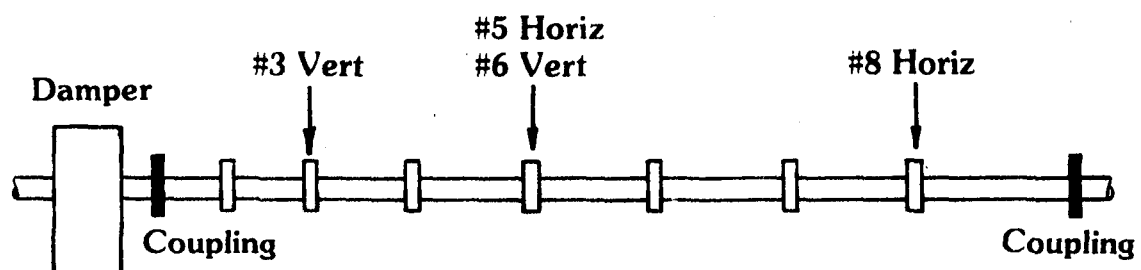


Figure 39 Rig Configuration with Instrumentation

792038

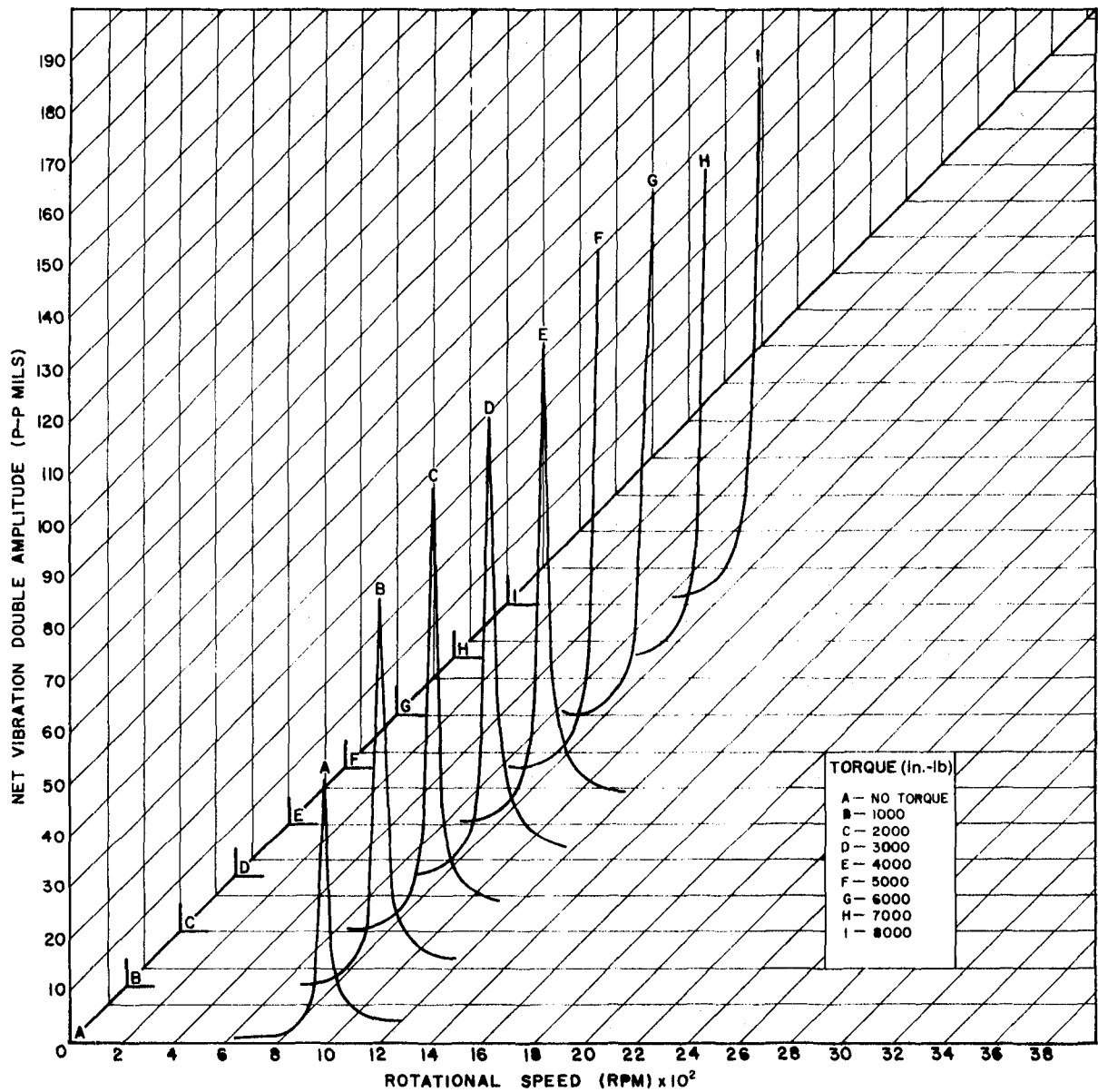


Figure 40 Baseline Test Condition - Probe 6  
(balanced without torque)

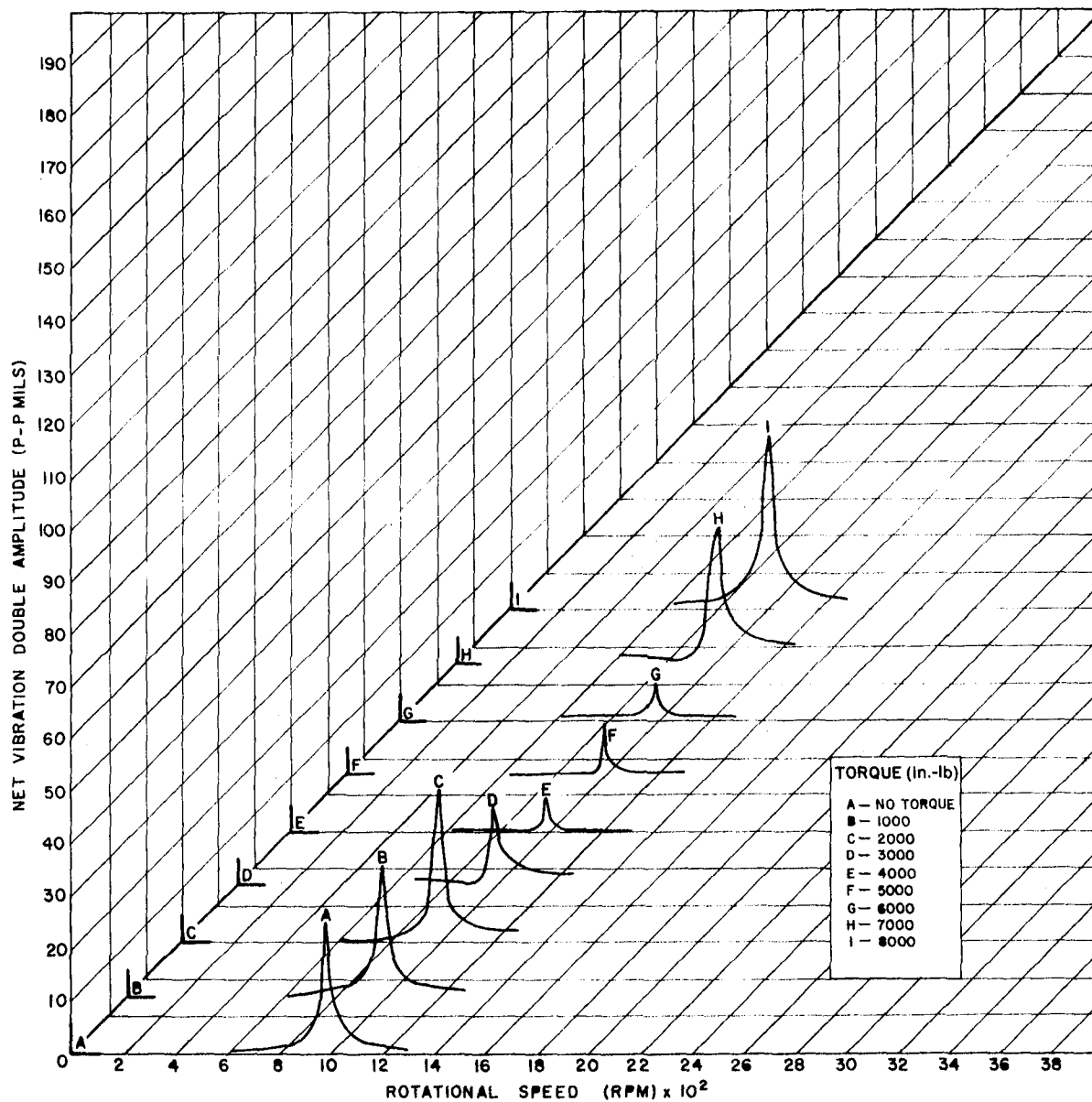


Figure 41 Rotor Response After Balancing Correction Applied for Torque Condition - Probe 8

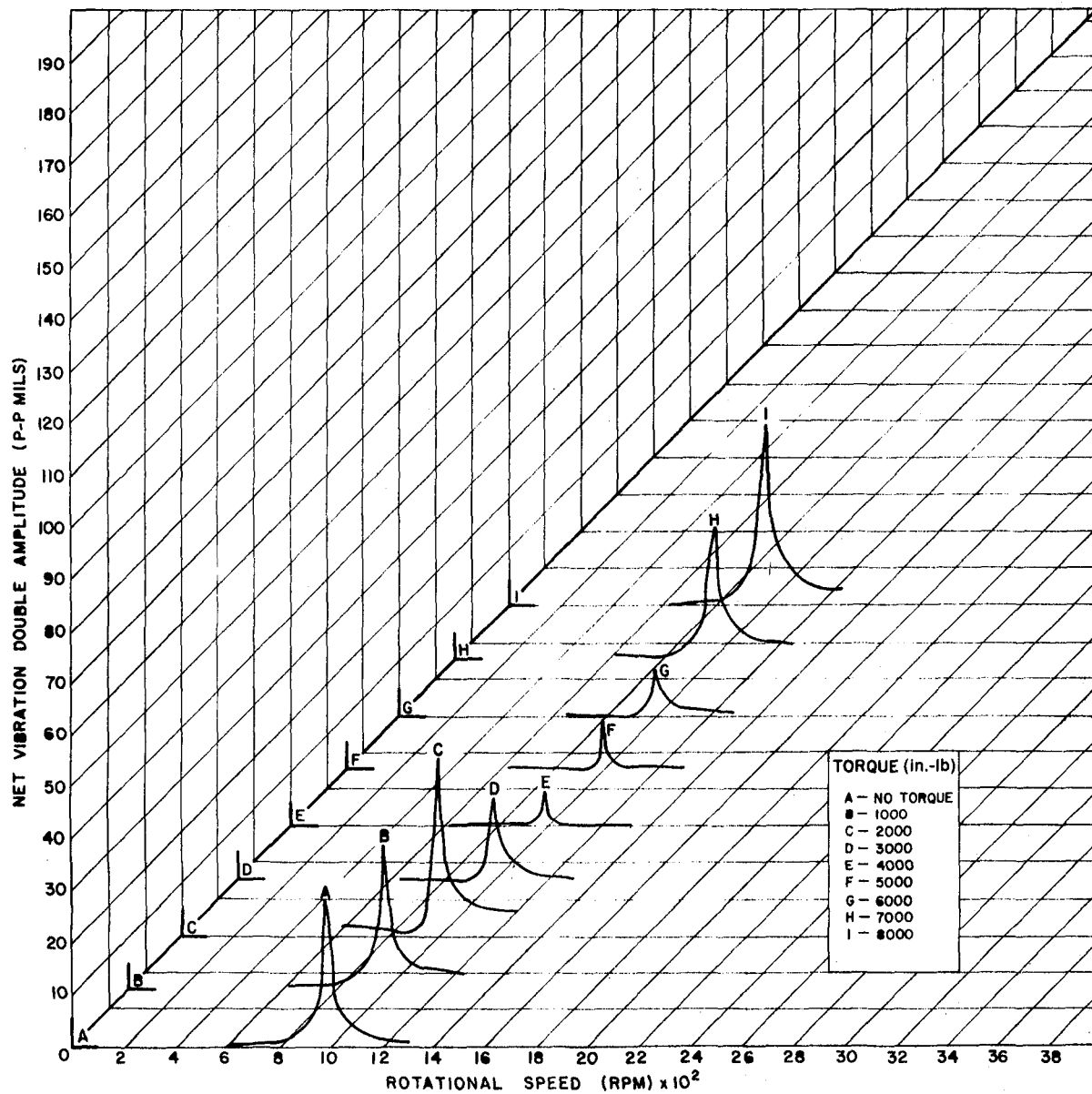


Figure 42 Rotor Response After Balancing Correction Applied for Torque Condition - Probe 3

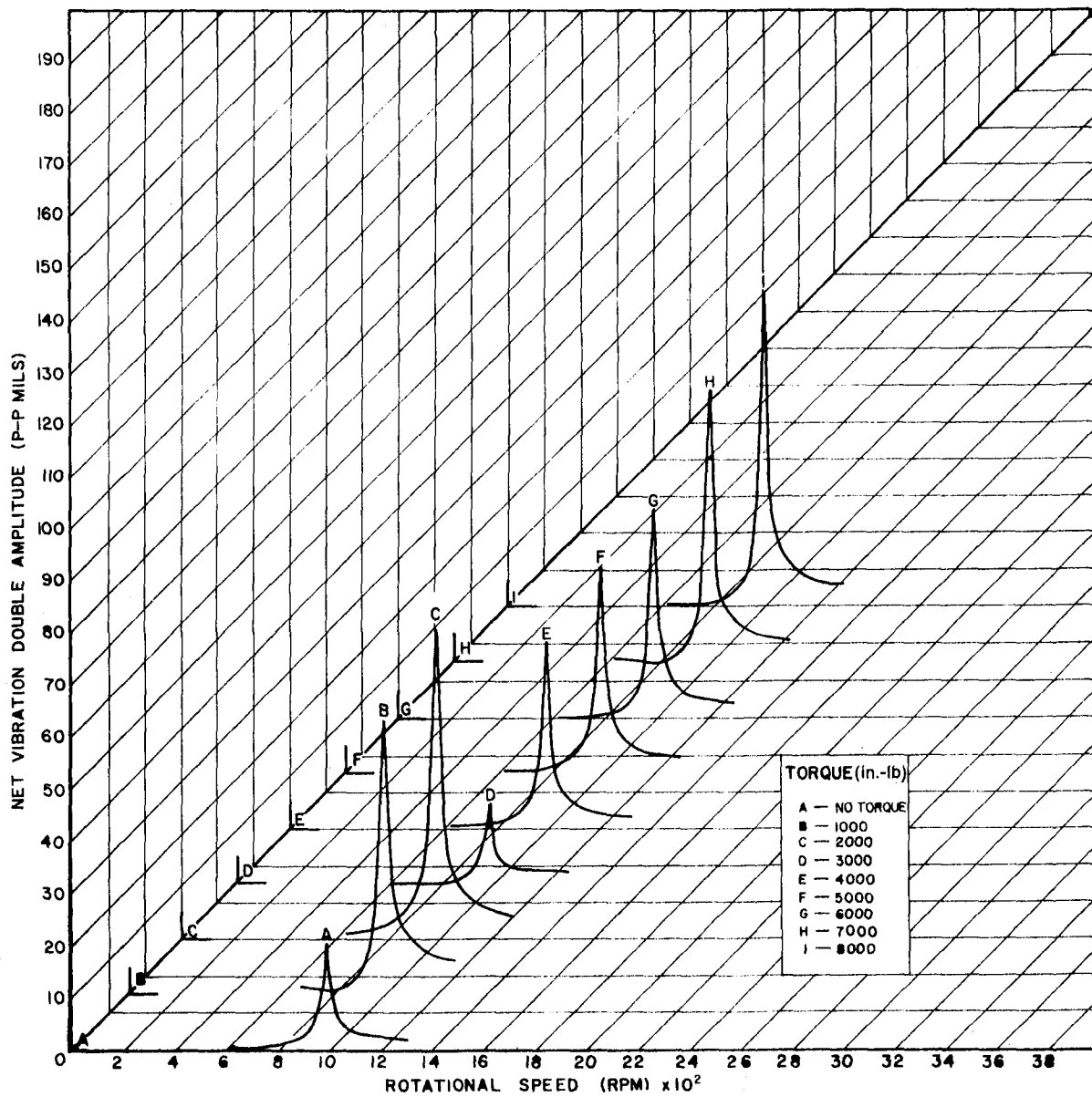


Figure 43 Rotor Response After Balancing Correction Applied for Torque - Probe 5

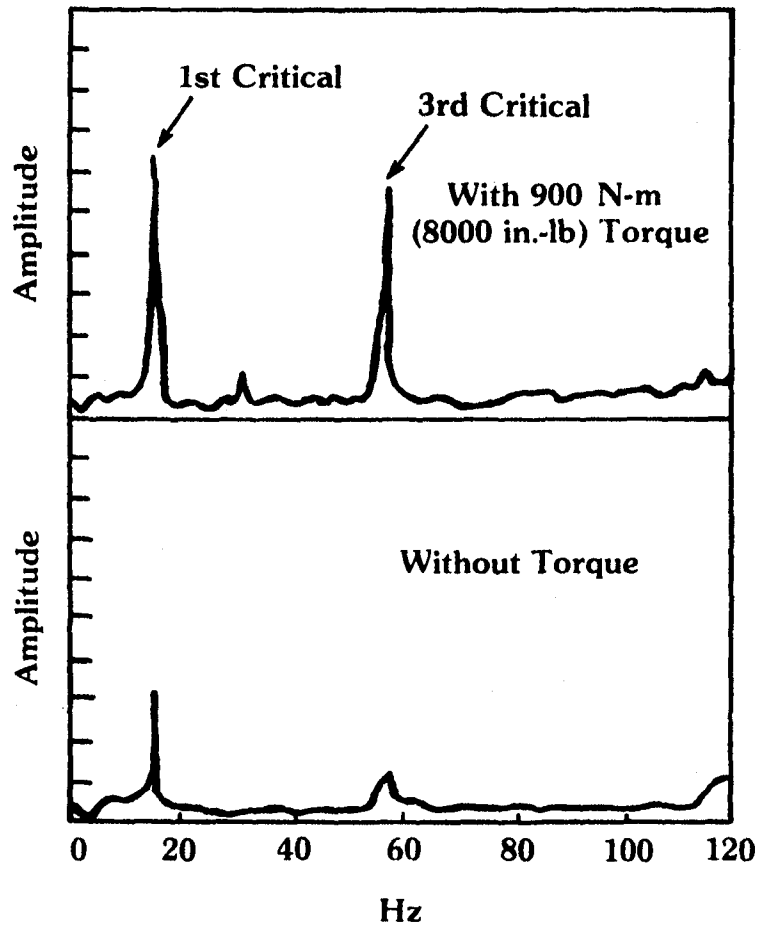


Figure 44 Typical Synchronous Response of Power Transmission Shaft With and Without Torque Loading

792037



## TABLES

**This Page Intentionally Left Blank**

TABLE 1  
4340 FATIGUE DATA  
Minimum/Maximum Stress R = .05

<u>Specimen Identification</u>	<u>Maximum Stress, Ksi</u>	<u>Cycles to Failure</u>
Smooth Specimens		
40-1	120	4,760,000 <sup>(1)</sup>
40-2	145	106,000
40-3	135	1,983,000
40-4	140	4,609,000
40-5	145	2,999,300
40-6	150	102,200
40-7	150	86,020
40-8	140	12,400,000 <sup>(1)</sup>
40-9	145	124,600
Laser-Burned Specimens		
40L-1	155	6,650
40L-2	132	10,730
40L-3	100	21,200
40L-4	50	119,900
40L-5	35	10,600,000 <sup>(1)</sup>
40L-6	50	140,300
40L-7	42.5	213,400
40L-8	37.5	380,900
40L-9	35	10,583,300 <sup>(1)</sup>
40L-10	37.5	290,500

(1) Specimen did not fail

TABLE 2

17-4 PH FATIGUE DATAMinimum/Maximum Stress R = .05

<u>Specimen Identification</u>	<u>Maximum Stress, Ksi</u>	<u>Cycles to Failure</u>
Smooth Specimens		
174-1	145	8,238,200
174-2	155	119,500
174-3	150	3,417,800
174-4	155	4,076,600
174-5	160	191,000
Laser-Burned Specimens		
174L-1	50	202,400
174L-2	50	174,500
174L-3	42.5	275,200
174L-4	37.5	375,500
174L-5	35	532,600
174L-6	30	757,800
174L-7	20	13,025,400 <sup>(1)</sup>
174L-8	25	1,703,300
174L-9	25	1,668,300
174L-10	30	774,200

(1) Specimen did not fail

TABLE 3  
INCONEL 718 FATIGUE DATA  
Minimum/Maximum Stress R = .05

<u>Specimen Identification</u>	<u>Maximum Stress Ksi</u>	<u>Cycles to Failure</u>
Smooth Specimens		
718-1	160	65,200
718-2	155	76,300
718-3	145	121,200
718-4	130	174,500
718-5	110	669,700
718-6	95	978,100
718-7	80	4,091,500
718-8	70	12,238,300 <sup>(1)</sup>
Laser-Burned Specimens		
718L-1	50	276,300
718L-2	35	1,655,700
718L-3	30	4,259,400
718L-4	27.5	5,397,400
718L-5	25	11,048,400 <sup>(1)</sup>
718L-6	35	1,575,400
718L-7	30	2,597,500
718L-8	27.5	2,946,800
718L-9	42.5	905,200
718L-10	25	5,519,100

(1) Specimen did not fail

TABLE 4  
6061-T6 FATIGUE DATA  
Minimum/Maximum Stress R = .05

<u>Specimen Identification</u>	<u>Maximum Stress, Ksi</u>	<u>Cycles to Failure</u>
Smooth Specimens		
60-1	28	8,900,000 <sup>(1)</sup>
60-2	37.5	1,067,900
60-3	32.5	7,018,100
60-4	35	3,770,000
60-5	37.5	2,334,600
60-6	35	5,444,600
60-7	32.5	4,968,800
60-8	30	20,339,500 <sup>(1)</sup>
60-9	35	7,671,500
60-10	32.5	12,430,000
Laser-Burned Specimens		
60L-1	8	4,064,500
60L-2	10	2,247,900
60L-3	12	1,661,500
60L-4	6.5	8,041,500
60L-5	5.5	29,236,300
60L-6	10	3,204,800
60L-7	15	1,075,300
60L-8	12	2,377,500
60L-9	6.5	6,087,400
60L-10	8.0	5,797,300

(1) Specimen did not fail

TABLE 5

FATIGUE STRENGTH REDUCTION FACTORS

Material	Fatigue Strength, $S_{\max}$ at $10^7$ cycles		Fatigue Strength Reduction Factors $K_f$
	Smooth	Laser-Burned	
4340	131.8 Ksi	35.0 Ksi	3.75
17-4 PH	144.9	20.0	7.25
Inconel 718	66.8	22.4	3.0
6061-T6	32.1	6.4	5.0

TABLE 6

COMPARISON OF STRESS CONCENTRATION FACTOR  $K_t$  TO FATIGUE STRENGTH REDUCTION FACTOR  $K_f$ 

Material	Groove Depth t (in.)	Groove Radius r (in.)	Calculated Stress Concentration Factor, $K_t$	Measured Fatigue Strength Reduction Factor, $K_f$ (Table 5)	$\frac{K_t}{K_f}$
4340	0.047	0.0275	3.61	3.75	1.0
17-4PH	0.052	0.027	3.78	7.25	0.5
Inconel 718	0.049	0.0275	3.67	3.0	1.2
6061-T6	0.094	0.032	4.43	5.0	0.9



TABLE 7

BASELINE DATA (FIGURE 40) AT 905 rpm

<u>Location</u>	<u>No Torque</u>		<u>900 N-m Torque</u>	
	<u>Orbit Radius</u> <u>mm (mil)</u>	<u>Orbit Phase</u> <u>degrees</u>	<u>Orbit Radius</u> <u>mm (mil)</u>	<u>Orbit Phase</u> <u>degrees</u>
3	0.16 (6.2)	290	1.24 (48.6)	22.9
5	0.51 (20.1)	288	1.40 (5.53)	25.2
6	0.53 (21.0)	287	1.71 (67.4)	35.5
8	0.40 (16.0)	290	1.26 (59.6)	21.5

TABLE 8

BALANCED ROTOR (FIGURES 41 and 42) AT 905 rpm

Correction weight 1.63 Grams at 316°

Location	Measured		Predicted					
	No Torque		With 900 N-m Torque		No Torque		With 900 N-m Torque	
	Orbit Radius mm (mils)	Orbit Phase degrees	Orbit Radius mm (mils)	Orbit Phase degrees	Orbit Radius mm (mils)	Orbit Phase degrees	Orbit Radius mm (mils)	Orbit Phase degrees
3	0.58 (22.9)	261	0.62 (24.2)	343	0.56 (22.0)	235	0.60 (23.6)	349
5	0.91 (35.6)	268	0.87 (34.4)	329	0.80 (32.3)	249	0.78 (30.8)	335
6	0.72 (28.2)	252	0.72 (30.4)	347	0.84 (33.0)	226	0.68 (26.6)	353
8	0.62 (24.3)	266	0.75 (29.5)	333	0.67 (26.5)	346	0.69 (27.5)	336

TABLE 9

PREDICTED BALANCING DATA

Correction Weight 2.68 Grams at 313°

<u>Location</u>	<u>No Torque</u>			<u>900 N-m Torque</u>		
	<u>Orbit Radius mm(mils)</u>	<u>Orbit Phase degrees</u>	<u>Weighting Value</u>	<u>Orbit Radius mm(mils)</u>	<u>Orbit Phase degrees</u>	<u>Weighting Value</u>
3	1.00 (39.3)	220°	0.0001	0.34 (13.2)	296°	1.0
5	1.26 (49.6)	230°	0.0001	0.57 (22.3)	291°	1.0
6	1.49 (58.7)	216°	0.0001	0.35 (13.9)	277°	1.0
8	1.08 (42.4)	227°	0.0001	0.46 (18.7)	291°	1.0

Correction Weight 0.616 grams at 333°

3	0.30 (11.7)	293°	1.0	1.03 (40.6)	4.08°	0.0001
5	0.60 (23.7)	291°	1.0	1.23 (48.3)	354°	0.0001
6	0.34 (13.6)	278°	1.0	1.31 (51.6)	8.1°	0.0001
8	0.48 (18.9)	292°	1.0	1.11 (43.8)	354°	0.0001

TABLE 10

INFLUENCE COEFFICIENT DATA  
FOR CENTER PLANE TRIAL WEIGHT

<u>Measurement Location</u>	<u>Real Component</u>	<u>Imaginary Component</u>
3	-4.151	-17.303
5	-5.223	-19.678
6	-5.928	-24.675
8	-5.342	-17.597

APPENDIX A

MATERIAL CERTIFICATIONS

**This Page Intentionally Left Blank**

58659



## COULTER STEEL &amp; FORGE COMPANY

Special Metals in Bars and Forgings

MAILING ADDRESS: P.O. BOX 8008  
1494 - 67TH STREET, EMERYVILLE, CALIFORNIA 94662  
415 - 653-2512 TELEX 33-6406 TWX 910-366-72931228 RIO VISTA AVENUE  
LOS ANGELES, CALIF. 90023  
TELEX 67-7340  
PHONE 213-261-6115334 WEST 8TH SOUTH  
SALT LAKE CITY, UTAH 84101  
TELEX 38-8330  
PHONE 801-322-35332715-6TH AVENUE SOUTH  
SEATTLE WASH 98134  
TELEX 32-9463  
PHONE 206-622-6086MECHANICAL TECHNOLOGY  
968 Albany - Shaker Road  
Latham, New York 12110

CUSTOMER'S ORDER NO.

902-00098

ORDER DATE

78 DEC 01

SAME

CUSTOMER ACCT. NO.

791061

INV REQ'D

SPEC CLAUSES

3

TAXABLE

NON-TAXABLE

X

CALL

OUR TRUCK

PREPAY

COLLECT

X

VIA

T

DATE SHIPPED

PARTIAL

COMPLETE

ITEM  
NO.QUANTITY  
ORD. SHIP

DESCRIPTION

Forged Alloy Steel, AISI 4340, Quenched at 1550°F,  
Oil Quenched & Tempered @ 1000°F, 4 hrs., A.C. Approx.  
Hardness Rc 37.

2

5

PCS. TF: 6-1/8"OD, 4-1/4"ID, 6.0"Thick

MARKING AND PACKAGING REQUIREMENTS

CSF STD

METALLURGICAL REPORT REQUIREMENTS

NOTARIZE

W/SHIPMENT

W/B LADING

TOTAL

MAIL COPIES TO:

## METALLURGICAL REPORT

Item  
No.Heat No.  
or Ident.

C.

Mn.

P.

S.

Si.

Cr.

Ni.

Mo.

Cu

G/S

15158

.40

.80

.008

.003

.29

.79

1.84

.26

.14

6/8

(Analyses are in percent)

Item  
No.Hardness  
of Material  
Supplied

Tensile

Yield  
—% Offset

El.

R.A.

BHN.

Size of  
Raw Stock

Mill

Rc 37

8"RCS Timken

Mag. Part. AMS 230TE

Freq .03/Sev .02

Macro = to or better

than S2-R2-C3 IAW

ASTM E-381 MIT-Std

430A

Item  
No.

Standard Jominy Hardenability Test Results—Sixteenths

1	2	3	4	5	6	8	10	12	14	20	24	28	32
60	59	59	59	58	58	58	58	58	57	57	57	56	56

We certify that the material described herein has been inspected and/or tested for conformance to the applicable specifications. Our warranty of quality provides for replacement only of any part of this material which subsequent inspection, test or use shows non-conformance with the specification. Inspection records, certifications, chemical and/or physical test reports are on file for your examination at EMERYVILLE, CALIFORNIA.

COULTER STEEL &amp; FORGE COMPANY

By

MANAGER, QUALITY CONTROL

Title

58660



## COULTER STEEL &amp; FORGE COMPANY

*Special Metals in Bars and Forgings*

MAILING ADDRESS, P.O. BOX 8008

1494 - 67TH STREET, EMERYVILLE, CALIFORNIA 94662

415 - 653-2512 TELEX 33-6406 TWX 910-366-7293

1228 RIO VISTA AVENUE

LOS ANGELES, CALIF. 90023

TELEX 67-7340

PHONE 213-261-6115

334 WEST 8TH SOUTH

SALT LAKE CITY, UTAH 84101

TELEX 38-8330

PHONE 801-322-3533

2715 6TH AVENUE SOUTH

SEATTLE, WASH. 98134

TELEX 32-9463

PHONE 206-622-6086

MECHANICAL TECHNOLOGY  
968 Albany - Shaker Road  
Latham, New York 12110

CUSTOMER ACCT NO

791061

INV REQD

SPEC CLAUSE

3

TAXABLE

NON-TAXABLE

X

CUSTOMER'S ORDER NO.

902-00098

ORDER DATE

78 DEC 01

CALL

OUR TRUCK

PREPAY

COLLECT

X

VIA

T  
DATE SHIPPED

SAME

ITEM  
NO.QUANTITY  
ORD. SHIP

DESCRIPTION

PARTIAL

COMPLETE

Forged Stainless Steel, Type 17-4PH, Solution Heat  
Treated at 1900°F, 1/2 hr. A.C. and Aged at 1025°F,  
4 hrs., A.C.

3

4

PCS. TF: 6-1/8"OD, 4-1/4"ID, -6.0"Thick

MARKING AND PACKAGING REQUIREMENTS

CSF STD

METALLURGICAL REPORT REQUIREMENTS

NOTARIZE

W/SHIPMENT

W/SH LADING

TOTAL

2

1

MAIL COPIES TO:

## METALLURGICAL REPORT

Item  
No.Heat No.  
or Ident.

C.

Mn.

P.

S.

Si.

Cr.

Ni.

Mo.

Cu

G/S

Ladle

76829

.038

.56

.030

.007

.42

16.06

4.68

.25

3.19

Co

Ta

Cb

.14

.01

.30

(Analyses are in percent)

Item  
No.Hardness  
of Material  
Supplied

Tensile

Yield  
--% Offset

El.

R.A.

BHN.

Size of  
Raw Stock

Mill

Bhn 363

8"SQ

Joslyn

We certify that the material described herein has been inspected and/or tested for conformance to the applicable specifications. Our warranty of quality provides for replacement only of any part of this material which subsequent inspection, test or use shows non-conformance with the specification. Inspection records, certifications, chemical and/or physical test reports are on file for your examination at EMERYVILLE, CALIFORNIA.

COULTER STEEL &amp; FORGE COMPANY

By

Frank Reim

Title

MANAGER, QUALITY CONTROL



## SCHLOSSER FORGE COMPANY

11711 ARROW ROUTE

CUCAMONGA, CALIFORNIA 91730

## METALLURGICAL ANALYSIS REPORT

HTL #94889.		CONDITION OF FORGINGS		FORGINGS FLUORESCENT PENETRANT INSPECTED PER:														
Solution treat @ 1925°F - 1 hr. - o/c, age @ 1400°F - 10 hrs.		FORGINGS MAGNETIC PARTICLE INSPECTED PER:																
Furnace cool to 1200°F, hold @ 1200°F for total age time of 20 hrs. @ Aircraft Heat Treating Co. Rough Machined.		FORGINGS ULTRASONIC INSPECTED PER:																
FORGINGS RADIOGRAPHICALLY INSPECTED PER:																		
MECHANICAL PROPERTY ACCEPTANCE OF LISTED FORGINGS ARE BASED ON RESULTS FROM:		<input type="checkbox"/> SECTIONED FORGINGS OR ROLLED RING <input type="checkbox"/> INTEGRAL TEST RING OR SLUG		PER: <input type="checkbox"/> LOT <input checked="" type="checkbox"/> HEAT <input type="checkbox"/> FORGING DATA SOURCE <input type="checkbox"/> S F C <input checked="" type="checkbox"/> MILL														
DELIVERY MEMO No. 14339 REFER TO THIS NO IN ALL CALLS AND CORRESPONDENCE	SOLD TO: Mechanical Technology, Inc. 968 Albany-Shaker Road Latham, New York 12110 Howard Robinson	SHIP TO: Same		VENDOR CODE														
SHOP ORDER NO. 3-1694	CUSTOMER ORDER NO. 902-00104	METHOD American Airlines 7365 1432	INVOICE DATE 2/19/79	DATE SHIPPED 2/19/79	RESALE TAXABLE QUANTITY SHIPPED 4													
MATERIAL Inco 718		PART NO. OR DESCRIPTION + .125 + .000 + .125 6.25 -.000 O.D. x 4.25-.125 I.D. x 6.00 -.000 LG		SPECIFICATIONS														
IDENTIFICATION			CHEMICAL ANALYSIS															
MILL	HEAT NO.	CODE	C	MN	P	S	SI	CR	MO	NI	AL	TI	CU	FE	CB/TA	Co	XX	XX
Teledyne Allvac	L 94		.037	.13	.003	.001	.01	18.25	2.95	52.50	.51	.99	.02	18.59	.22	.26	B	.004
						(Analyses are in percent)												
SERIAL	CODE	TENSILE						STRESS RUPTURE						BHN	Gr 5A			
		TEST LOCATION & DIRECTION		TEMP OF	YIELD -% OFF. KSI	ULTIMATE KSI	% ELONG. IN 4 D	% RED OF AREA	S R	STRESS KSI	TEMP. OF	HRS. TO BREAK	% ELONG. IN 4 D			INCREASE STRESS TO		
																		415
REMARKS: TELEPHONE (714) 987-4760										CODE		CLEANLINESS AMS FREQ SEV.		JOMINY HARDENABILITY ROCKWELL "C" SCALE IN 1/16"				
COPIES OF ACTUAL TEST REPORT SHOWING CONFORMANCE TO APPLICABLE SPECIFICATIONS ARE ON FILE AT OUR PLANT AND ARE AVAILABLE FOR REVIEW BY YOU OR YOUR REPRESENTATIVE - WE HEREBY CERTIFY THESE FORGINGS HAVE BEEN TESTED, INSPECTED AND ACCEPTED IN ACCORDANCE WITH THE APPLICABLE BLUE PRINTS AND SPECIFICATIONS.																		

I CERTIFY THAT TO THE BEST OF MY KNOWLEDGE AND BELIEF THIS MATERIAL ANALYSIS REPORT IS TRUE AND CORRECT.

Carol Robinson  
METALLURGIST



### Special Metals in Bars and Forgings

MAILING ADDRESS, P.O. BOX 8008

1494 - 67TH STREET, EMERYVILLE, CALIFORNIA 94662

415 - 653-2512 TELEX 33-6406 TWX 910-366-7293

1228 BND VISTA AVENUE

374 WEST 8TH SOUTH

2715-6TH AVENUE SOUTH

1220 TWO VISTA AVENUE  
LOS ANGELES, CALIF 90023

SALT LAKE CITY, UTAH 84101

SEATTLE WASH 98134

TELEFAX 67-7340

LAKE CITY, UTAH  
TELEFAX 30.8330

TELEX 32-9463

PHONE 213-261-6115

PHONE 801-322-3533

PHONE 206-622-6086

## ALUMINUM AND ITS ALLOYS

We certify that the material described herein has been inspected and/or tested for conformance to the applicable specifications. Our warranty of quality provides for replacement only of any part of this material which subsequent inspection, test or use shows non-conformance with the specification. Inspection records, certifications, chemical and/or physical test reports are on file for your examination at EMERYVILLE, CALIFORNIA.

COULTER STEEL &amp; FORGE COMPANY

By Frank Kloss

MANAGER, QUALITY CONTROL

Title \_\_\_\_\_

APPENDIX B

SPECIMEN MACHINING DETAILS

**This Page Intentionally Left Blank**

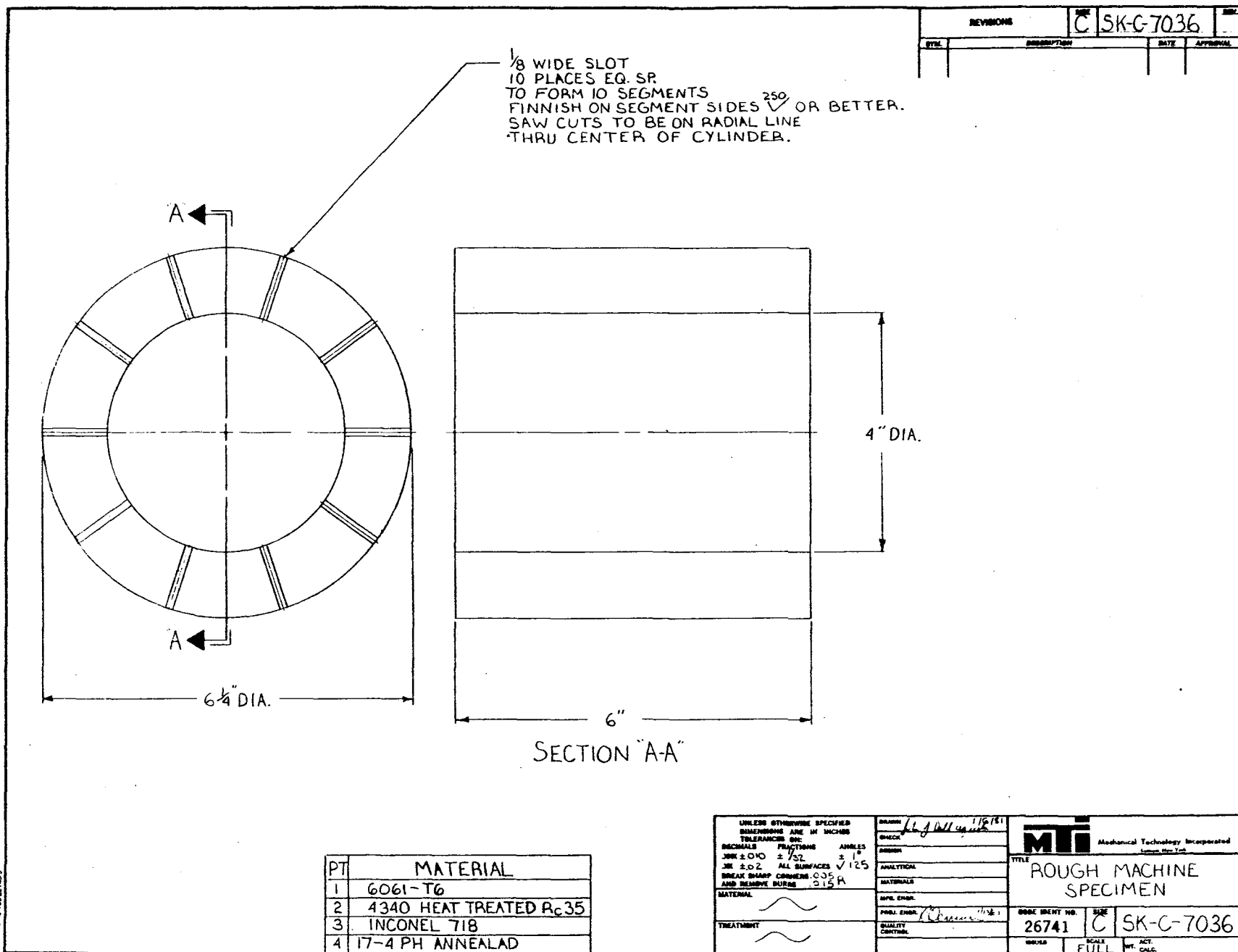
## PROCEDURE FOR GRINDING RADIUS OF HIGH CYCLE FATIGUE SPECIMENS

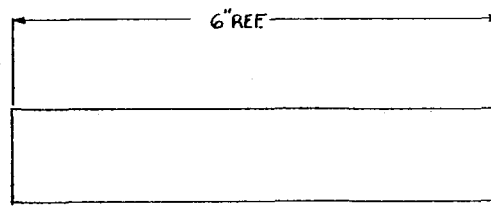
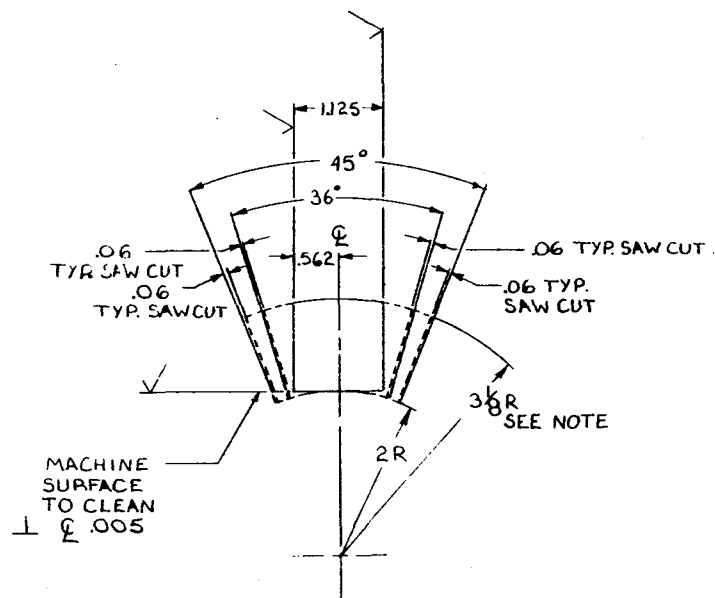
1. Surface grind with a contoured wheel by removing small amounts of material until .005 inch excess remains.
2. The next .004 inch should be removed by surface grinding at a rate of no more than .0002 inch per pass.
3. The final .001 inch should be removed by polishing\* longitudinally to impart a maximum of eight microinch surface roughness.
4. After polishing, all remaining grinding and polishing marks should be longitudinal. No transverse grinding marks should be evident when viewed at 20X magnification.
5. The finished specimen should be degreased.

---

\*Longitudinally means in a direction parallel to the long dimension of the specimen. Extreme caution should be exercised in polishing to ensure material is properly removed rather than merely smeared to produce a smooth surface.







NOTES:

1.  $\frac{3}{8}$  RADIUS NOT TO BE MODIFIED.
2. MATERIAL SPECIFIED, SK-WTA 92179.
3.  $\frac{32}{\sqrt{}}$  OR BETTER ON SURFACES INDICATED.
4. DASHED LINES INDICATE MATERIAL TO BE REMOVED FROM EITHER 36° OR 45° SAWED SEGMENTS.

UNLESS OTHERWISE SPECIFIED DIMENSIONS ARE IN INCHES		DATE: 11/17/79		REV: C	
TOLERANCES ON: DIMENSIONS FRACTIONS ANGLES INCH ± .005 ± 1/64 ± 1° JUN ± .01 ALL SURFACES √32 BREAK SHARP CORNERS .005 R AND REMOVE BURRS .015 R		DRAWN: H. J. [signature]		SK-C-7038	
MATERIAL: SEE NOTES		ANALYSIS:		TITLE: LASER BURN	
TREATMENT: [wavy line]		MATERIALS:		TEST SPECIMEN	
QUALITY CONTROL:		PUBL. ENGR. [signature]		CODE IDENT NO. 26741	
		ISSUED:		SCALE: FULL	
				ACT. DATE:	





